TECHNISCHE UNIVERSITÄT DRESDEN

FACULTY OF ENVIRONMENTAL SCIENCES
DEPARTMENT OF HYDRO SCIENCES
INSTITUTE OF HYDROLOGY AND METEOROLOGY
CHAIR OF HYDROLOGY
PROF. DR. NIELS SCHÜTZE

Master's Thesis

# 2D hydraulic modelling of a braided river system using aerial imagery for water depth mapping: The Wairau River, New Zealand

Mohamed Adil Osman Elbashir

Supervisor: Dr. Thomas Wöhling

Dresden, September 2019

# Declaration of independence

I, hereby declare that I have submitted my thesis to the Examination Board of the Department of Hydro Science, Faculty of Environmental Science today on the subject:

*2D hydraulic modelling of a braided river system using aerial imagery for water depth mapping: The Wairau River, New Zealand*

I have written it completely independently and have not used any other sources or aids than those indicated and have not identified quotations.

Dresden, 02/09/2019

Mohamed Adil Osman Elbashir

## Abstract

In this study, a 2D quasi-unsteady state modelling was performed at five characteristic discharges on a 23.5 km reach of the lower Wairau River in order to quantify its hydraulic geometry. A high-resolution multispectral Aerial image was used in depth mapping. Good linear correlation ($R^2$ = 0.744) was obtained between the measured depth from survey data and a band-ratio value from the image. The depth retrieval accuracy was $\sigma_d$= 0.206 m (25% sample mean depth) with an underestimation for high depth values (>1.25) up to 15% at $d_{max}$= 2.15 m. The image-derived depth value was then used to adjust the DEM layer, which represent the model geometry. The model was calibrated at low and median flow for the optimum Manning's value (n = 0.03) by comparing simulated vs observed hydrographs at three gauging stations. The frequency distribution of the simulated velocity was bi-modal distribution with modal velocity = 0.91*mean velocity and was in range of regional values. The frequency distribution of simulated depth was positively skewed similar to regional trend but the modal depth was much lower value at 0.1*mean depth. The reach averaged hydraulic geometry relations were more consistent for all reaches and its exponents had less range (0.25-0.35) than the at-a-station hydraulic geometry exponents (0.22-0.56) did. They also scored better results on the continuity equation check. By comparing the overall reach averaged exponents to the regional values it is found that the width exponent (0.34, P=0.07) was significantly higher than the modal range (0.17-0.2, P = 0.43). This indicates that the study area reacts to increased river flow by higher changes in the water surface width than changes in velocity or water depth, compared to regional rates. As for comparing within the study area, the Upper reach reacts to increased river flow by higher changes in width, the lower reach by higher changes in depth and the middle reach by slightly higher changes in velocity.

# Table of Contents

## List of Figures

## List of tables

# 1 Introduction

## 1.1 Background

The braided river system is defined by (Ashmore, 2013) as an unstable connected network of channels that is divided by ephemeral bars. These bars require sizable bed load transport at threshold flows and processes of scour and deposition. It occurs naturally in unconfined flow conditions over non-cohesive, mobile sediments (Murray and Paola, 1994). Braided rivers are observed in a wide range of conditions, from Mountainous regions to alluvial fans, as well as in coastal and continental plains. They form whenever the geological, hydrological, and geomorphic conditions leads to coarse bed loads, high stream power and low erosion resistance of the channel material (Osterkamp, 1978). Figure (1) below shows the morphology of a braided river. Even though the morphology appears to be chaotic and unstable, but they have hydraulic geometry relations comparable to the single channel rivers. At the same time they have their own distinguishable statistical characteristics. The morphology is mainly described by the processes of bar formation and migration, as well as the dynamics of bifurcation and confluences of anabranches (Ashmore, 2013).

Figure 1 Photo of the braided River Rakaia, New Zealand. Courtesy of Bill Irwin (www.billirwinarts.com)

## 1.2 Motivation and objectives

The Wairau river plain have incurred significant modifications for flood protection purposes since the early 1900s (Wilson and Wöhling, 2015). The last major modification on the 1960s was by installing a stop-bank network which considerably confined the natural extent of the floodplain. As a result, the river's hydraulic properties have since being changing. This effect was also evident when examining the long term exchange rate with the underlying aquifer. However despite the river training, it still characterises as a braided river. Only now the hydraulic properties are in a transitional state that is poorly understood. The high economic and ecological importance of the Wairau floodplain raises the need for a better understanding and quantification the status quo dynamics.

The objective of this study is a better understanding of the flow-geometry relationship in the Wairau River flood plain. To that end, a 2D hydraulic simulation of the system is carried out at different flow levels. The model simulations will be used to derive relationships between flow and other hydraulic properties such as water depth, wetted perimeter but also the branch-channel ratio, sinuosity of the stream network, and the ratio between cross-directional flow and flow along the thalweg. Moreover, longitudinal profiles will better describe the change in hydraulic properties in areas of interest such as cross flow reaches and branching points.

Accurately representing the river-bed geometry in numerical models is a challenging and data intensive task. Episodic cross-sectional bathymetric survey data fails to capture the complex flow channel geometry (and their changes) in braided rivers. LiDAR data, on the other hand, provides high-resolution snapshots in time but doesn‘t penetrate water and thus doesn’t capture the bathymetry. To solve this issue, publically available, multispectral aerial imagery of the study area are used to derive a colour-water depth relationship. The relationship is then used to adjust the LiDAR data to obtain the final model geometry for the hydraulic simulations.

The study output is expected to provide some useful insights to model the aquifer interactions in the Wairau River. However, the consideration of river recharge is outside the scope of this study. The aquifer fluxes were only accounted for in the calibration and validation steps to avoid inaccuracies.

## 1.3 Thesis structure

*Chapter 2* briefly summarises the previous literature on the hydraulic modelling topic as well as on the image based depth mapping.

*Chapter 3* introduces the domain of the study area, the type and specifications of acquired data, the different tools used and a stepwise description of the approaches adopted to reach the results.

*Chapter 4* contains the key obtained results, presented in a graphical and tabular format for easier understanding, were each finding is followed by a short discussion about its interpretations, significance and sources of uncertainty.

*Chapter 5* concludes the thesis by summarising the main findings and suggestions for further work.

# 2 Literature review

## 2.1 On the hydraulic modelling of braided rivers

Over the last three decades, a lot of effort has been made in the field of braided systems to better understand the complex nature of the flow-geometry relationships. In particular, the laboratory-based physical modelling (e.g. Davoren and Mosley, 1986; Goff and Ashmore, 1994) offered valuable insights to the underlying hydraulic processes, especially on bed load transport. At the same time, few data acquisition missions provided a base for further statistical modelling (e.g. Hoey and Sutherland, 1991; Warburton, 1996). The numerical 2D models, on the other hand, were not introduced until later on. Such models provided a spatially distributed quantification on flow depth and velocity on the braid level (e.g Lane and Richards, 1998) as well as on the reach level (e.g. Thomas and Nicholas, 2002).

This study focused mainly on reviewing literature on the region of New Zealand, in order to adopt suitable approaches and draw comparisons. *Nicholas* (2003) simulated a braided reach on the Avoca River, South Island. His approach for analysis was based on the frequency distribution of the simulated hydraulics; namely mean flow depth and velocity. He found that there is a consistent trend of the frequency distributions compared to previous literature, and that there is a systematic change in the distribution shape with increasing discharges. He further argues that it could be used to develop statistical models for depth and velocity prediction on the reach scale. The Frequency distribution is therefore used here along with other methods. Another different approach was adopted by *Jowett* (1998). He calculated the hydraulic geometry relations for 73 New Zealand river reaches and compared their geometry exponents with the international mean values. The study found that -for New Zealand rivers- greater changes are observed in velocity than in depth values when increasing discharges. Moreover, he tested the prediction capability of these hydraulic relations in instream habitat assessment and found acceptable results. This study will therefore also obtain the hydraulic geometry exponents for the study region and compare it to *Jowett's* and to the mean international values. Moreover, these hydraulic geometry exponents provide both quantitative and qualitative description of the river hydraulics. *Singh* (2003) provided an extensive description of the different hydraulic geometry theories and mentioned that the width exponent (*b*) can be used to distinguish between braided, meandering or straight rivers.

Regarding the parameterization of braided river models, a recent study by *Williams et al.,* (2013) validated a hydraulic model in a highly data-rich environment. The study tested the effect of using a spatially uniform roughness parameter in calibration. As a model input, they used high-resolution topographic survey data and a high temporal resolution hydraulic data. Based on calibration and validation results, they concluded that using a spatially uniform roughness parameter produces acceptable results, both at the braid bar and at the reach scale. However, the study also found that the model is highly sensitive to the horizontal eddy viscosity parameter, which influences the cross-channel velocity and localization of high shear stress zones. This study therefore adopts a spatially uniform bed roughness parameterization, given the big extent of the study area.

## 2.2 On the image-based depth mapping

There is a wide range of literature found in the field of optical bathymetry of shallow rivers and lakes, whether it being active (laser-based) or passive (image-based) optical bathymetry. The earlier studies on image-based bathymetry in gravel-bed rivers were mostly empirical (e.g. Winterbottom and Gilvear,

1997; Westaway, Lane and Hicks, 2003). In other words, the fitted equations were not transferable to different study locations. Then later on, *Legleiter et al.,* (2004) introduced the physical basis of the radiative transfer processes in river environments, based upon previous studies in shallow marine environments. In his study, he assessed the accuracy of two depth retrieval algorithms. One is a linear transform algorithm originally introduced by *Lyzenga* (1978), and the other is a ratio-based algorithm used more recently by *Dierssen et al.*, (2003). His results indicated that the latter produced stronger correlation between the depth and the ratio of specific wavelengths. Then *Legleiter et al.,* (2009) went further and developed an algorithm for identifying the optimal pair of wavelengths to be used in the band-ratio equation. They found that the water surface roughness limits the use of NIR and Blue bands in depth retrieval, and that the optimal bands to form the ratio lie between them. The study also applied the band-ratio method using hyperspectral image data and resulted in an accurate bathymetry for a shallow river. It proves to be a simple and effective method in such conditions of shallow depth, clear water, reflective riverbed substrate and minimum atmospheric effects. Building on these results, *Legleiter* (2013) assessed the usage of three types of public domain multispectral images in river bathymetry. The study used a band-ratio algorithm between the Red (R) and the Green (G) bands that produced good results.

*Moretto et al.,* (2013) conducted a fluvial geomorphic changes study using hybrid DTM from merging LiDAR and image bathymetry. For the image bathymetry algorithm, he used an empirical linear equation using all three bands (RGB). He argues that all bands are strongly correlated to water depth according to statistical analysis carried in three gravel-bed streams. Although the results were highly correlated, the method is data intensive. The calibration points should be uniformly sampled over depths with a minimum of 250 points for each 0.2m step depth to produce a near LiDAR accuracy.

# 3 Tools and methods

## 3.1 Study area

The Wairau River is located at the northeastern end of the South island of New Zealand. The river originates at the Spenser Mountains and flows into the Pacific sea some 170 Km downstream at Wairau Bar. It drains a catchment area of around 3,582 $Km^2$ with elevations ranging from sea level to 2,309 m.a.s.l. (McMillan *et al.*, 2010). The study is carried out on the Wairau flood plains, Marlborough district, on a 23.5 Km long reach in the lower river part. The model boundary leis downstream of the Waihopai river confluence and upstream of the Wairau diversion channel at State highway-1 Bridge (Fig. 2). There the river is characterized as a braided, mobile gravel-bed river with a mean slope of around 2.7 ‰ (Wöhling *et al.*, 2018). The main channel mean width is around 100 m and the active floodplain mean width is around 800 m, confined by stop-banks and vegetated berms (Christensen and Doscher, 2010). The river is also connected to the Wairau aquifer. Based on historic and recent gauging, the river is feeding the aquifer for most of its length and gaining water at the lower reaches downstream of Wratts Road (Wöhling *et al.*, 2018). The values of the Average Annual low flow, Average Annual Mean Flow and the Average Annual Flood Flow corresponds to 12, 100 and 1800 $m^3/s$ respectively.

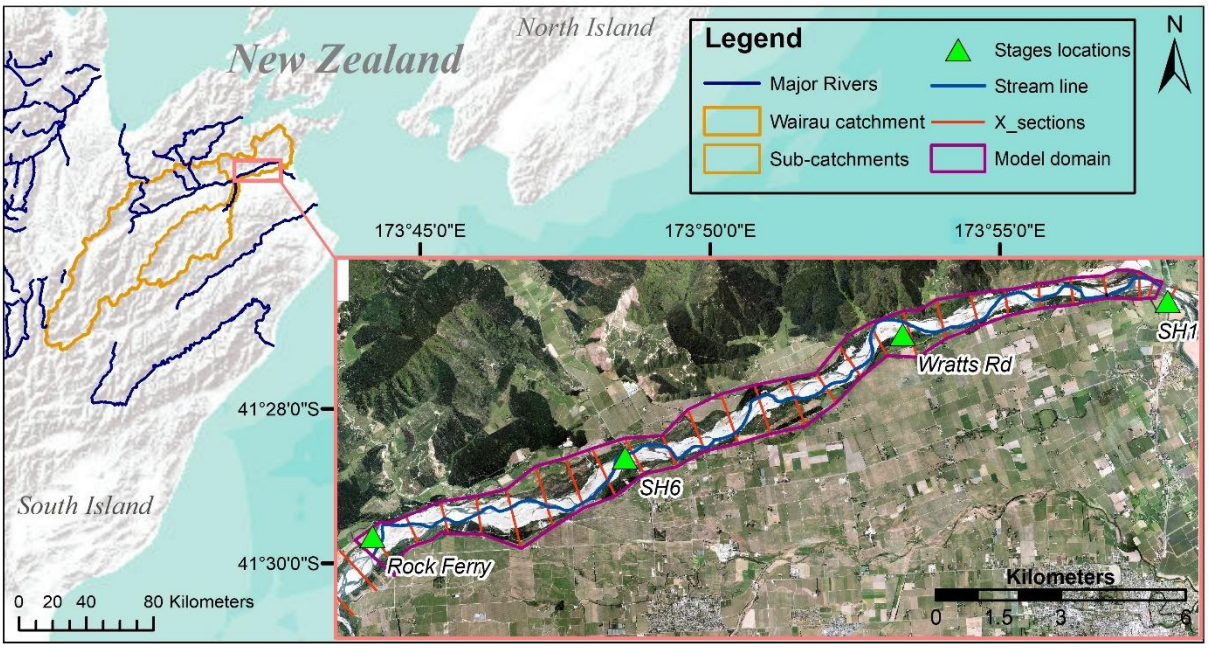


Figure 2 Study area, lower Wairau River

## 3.2 Data collection

### 3.2.1 Hydrological data

The hydrological data used were provided from the Marlborough District Council (MDC) at four gauging stations, namely, Rock Ferry, SH6, Wratts Rd and SH1 (Fig. 2). The first and last gauges provide the upper and lower boundary conditions of the study area and the other two are located at approximately one- and two-thirds of the reach length. At these locations, the riverbed undergoes

relatively minor changes and has a single channel in base flow conditions (Wilson and Wöhling, 2015). The time series data contains 15-minutes stage records as well as mean daily flow records at all stations from December 2013 up to 2018. Additionally, 15-min flow records are available at the long-term recorder SH1, which facilitated the construction of a relatively reliable rating curve from concurrent readings. For the other three temporary stations, rating curves were constructed from daily means. Unfortunately, only point locations of these stations are available and the exact cross-sections are unknown. They were drawn perpendicular to the active river braid at the time of simulation.

### 3.2.2 Geometrical data

A Digital Elevation Model (DEM) of LiDAR data were obtained from the Land Information New Zealand (LINZ) database for the year 2014. The LiDAR was acquired at low flow periods in February and May and the DEM has a 2.0m grid resolution with +/-0.06m height accuracy.

MDC has also conducted regular bathymetric survey from 1958 to 2012 in the lower Wairau River at fixed cross sections every 800 m apart. Data from 17 cross sections inside the study area were used from the latest Survey in 2012.

### 3.2.3 Aerial Imagery

The multi-spectral aerial photos of the region were also downloaded from the LINZ Data service in 960m*1440m gridded tiles. They were taken during December 2011 – April 2012. Imagery supplied as 40cm pixel resolution (0.4m GSD), 3-band (RGB) uncompressed GeoTIFF. The final spatial accuracy varies from +/-2.0m (@ 95% confidence) to +/-10m (@ 95% confidence).

## 3.3 River geometry construction approach

The main idea of geometry reconstruction is modifying the LiDAR data in submerged areas to represent riverbed elevations instead of water surface elevations. To that end, a statistically based color vs depth relationship is developed using aerial photos and survey data and then applied to create a water depth map for the river. This depth layer is then subtracted from the LiDAR layer to produce the final modified DEM used in the model. Below are the detailed steps adopted:

### 3.3.1 Processing of multi-spectral aerial photos

The photos are taken at favorable atmospheric conditions (i.e. overcast with no cloud cover) but over a long period, so correction is needed against atmospheric variations. The main variation is difference in sunlight radiation and angle depending on the day each region was scanned. The image processing software ERDAS IMAGINE provides a wide range of tools and was used to manage color correction. All photo tiles were combined in one Mosaic using Illumination Equalizing and Histogram Matching to account for sunlight correction. The final output image has a uniform illumination over the whole area and sun light radiation is assumed constant. Figure (3) below shows the aerial photos for part of the upstream Wairau plain, before and after atmospheric correction. Comparing the upper left corner in the two photos shows how the illumination is normalized across the study area.

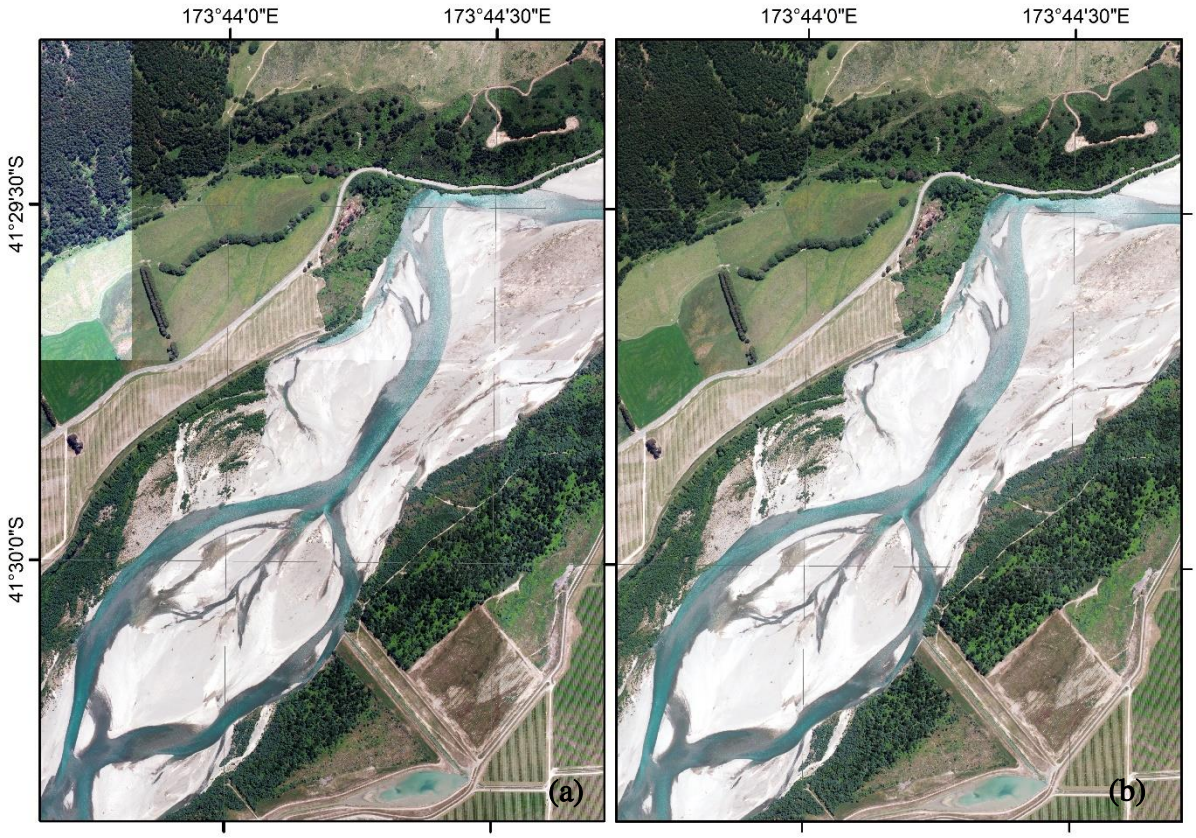


Figure 3 Aerial photos (a) before and (b) after atmospheric correction

### 3.3.2 Analysis and mitigation of survey data

The surveyed points has to be checked for both spatial and height accuracy against the LiDAR data. Spatially, the surveyed points' coordinates are available as distances along the cross section, and only the edge points of the cross section has known coordinates. Thus before converting the points to XY coordinates; they were checked for lateral shifts along every cross section. Using ArcMap, all cross sections' profiles were extracted from the LiDAR and plotted against the surveyed data points. A simple statistical tool was developed in excel to shift data points until the minimum height difference between the points and LiDAR is met. Some points laying on roads or embankments provided additional visual cross-referencing. Figure (4) shows the survey points for two cross-sections along with their profiles, at the downstream part of the study area. The second cross section shows an extreme case where the survey points are incorrectly shifted by more than 190m to the right side. After cross-referencing to LiDAR, all points XY coordinates where calculated.

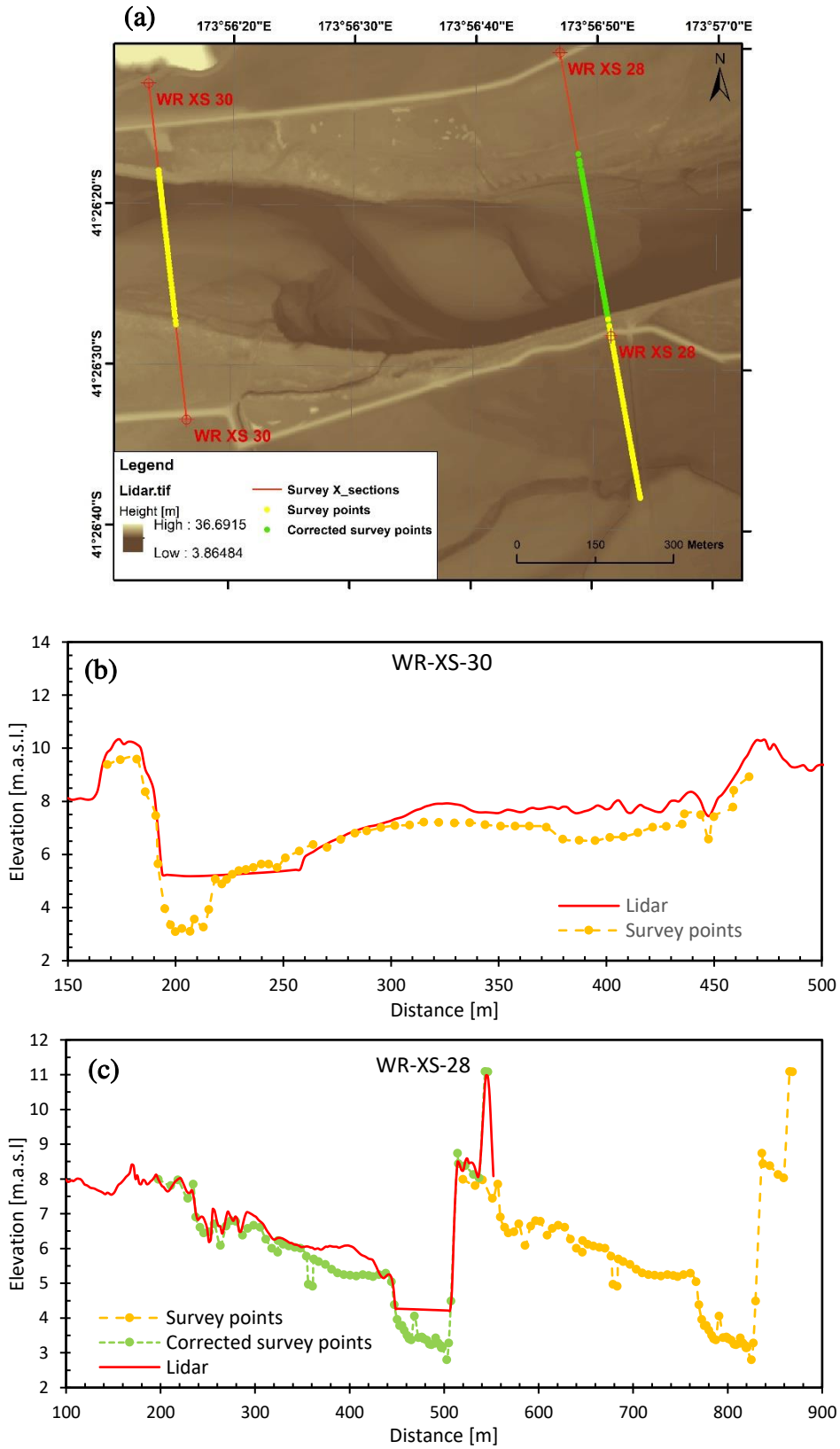


Figure 4 Coordinates correction for Survey data: (a) plan view, Survey cross sections (b) WR-30 and (c) WR-28

Secondly, the survey points were checked for systematic errors in height against the LiDAR data. ArcMap facilitated the classification of points into land points and water points. The average height difference of land points between Survey dataset and LiDAR dataset was then used to correct all points.

Constructing a statistically based band-value vs depth relationship: (constraint layers, layers alignment, point extraction, relation by x-section, split sample validation, depth layer creation)

After aligning all layers, the surveyed water depth ($d_S$) was considered for each water point as the height difference according to equation below:

$$d_S = Z_L - Z_S \tag{1}$$

Where $Z_L$ and $Z_S$ denotes the elevations from the LiDAR layer and Survey data layer respectively. Then the band values were extracted from the Aerial photo layer for the same points. The photo-derived band ratio X is defined as:

$$X = \ln(G/R) \tag{2}$$

Where G and R denotes the green and red band values respectively. Finally, the equation governing X and the image-derived water depth ($d_i$) is a simple linear regression equation defined as:

$$d_i = a * X + b \tag{3}$$

Where $a$ & $b$ are correlation parameters representing the slope and intercept of the regression line. Nevertheless, since the photo and LiDAR data were gathered from different years (i.e. 2012 and 2014), they are not perfectly aligned in some cross sections, which affects the linear regression. To avoid including points from these locations, regional depth vs X relationships were plotted for every cross-section individually to filter cross sections by comparing the slope and intercept of regression lines. Figure (5) below shows that while most of the regression lines have similar slope, others have inaccuracies. For example, major channel shift at XS62 lead to an inverse regression line slope. A smaller shift at XS54 and XS38 reduced the intercept, and sun glint on the water surface lead to both higher slope and intercept at XS42.

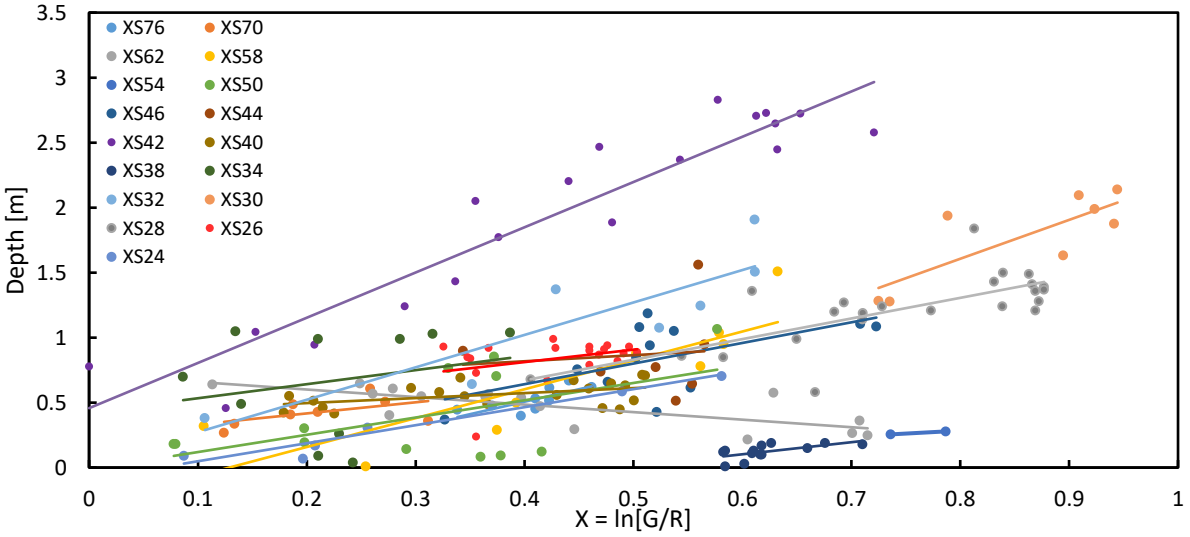


Figure 5 Filtering cross sections using local regression lines

After excluding points of inaccurate cross-sections, split sample analysis was conducted to the rest of the points (140 in total). The sample was randomly divided into two halves, taking into account that each half covers the whole depth range (0 – 2.5m). The first half (i.e. calibration dataset) is used to generate X vs depth relationship and the other half (i.e. validation dataset) was reserved to validate this relationship in depth retrieval accuracy. To test depth retrieval accuracy, the image-derived depth was

plotted vs survey depth for the validation dataset sample. Ideally, a line slope of value 1.0 (45° angle) and an vertical intercept value of 0.0 means unbiased prediction. Positive intercept value and/or slopes > 1.0 indicates overestimation while Negative intercept values and/or slopes <1.0 indicated underestimation.

For creating the depth map, all water pixels from the aerial photo were selected using the unsupervised classification tool in ArcMap. Then the equation derived above was applied on these pixels, producing a raster layer with depth values covering all water bodies. The different layers are shown in figure (7) below for the lower part of the study area.

### 3.3.3 Augmenting LiDAR and depth maps

As a final step, simple raster calculation was performed to subtract the depth layer from the LiDAR layer. The final DEM represents the whole flood plain geometry. Figure (6) below shows the profiles at selected cross sections for the geometry before and after depth mapping correction.

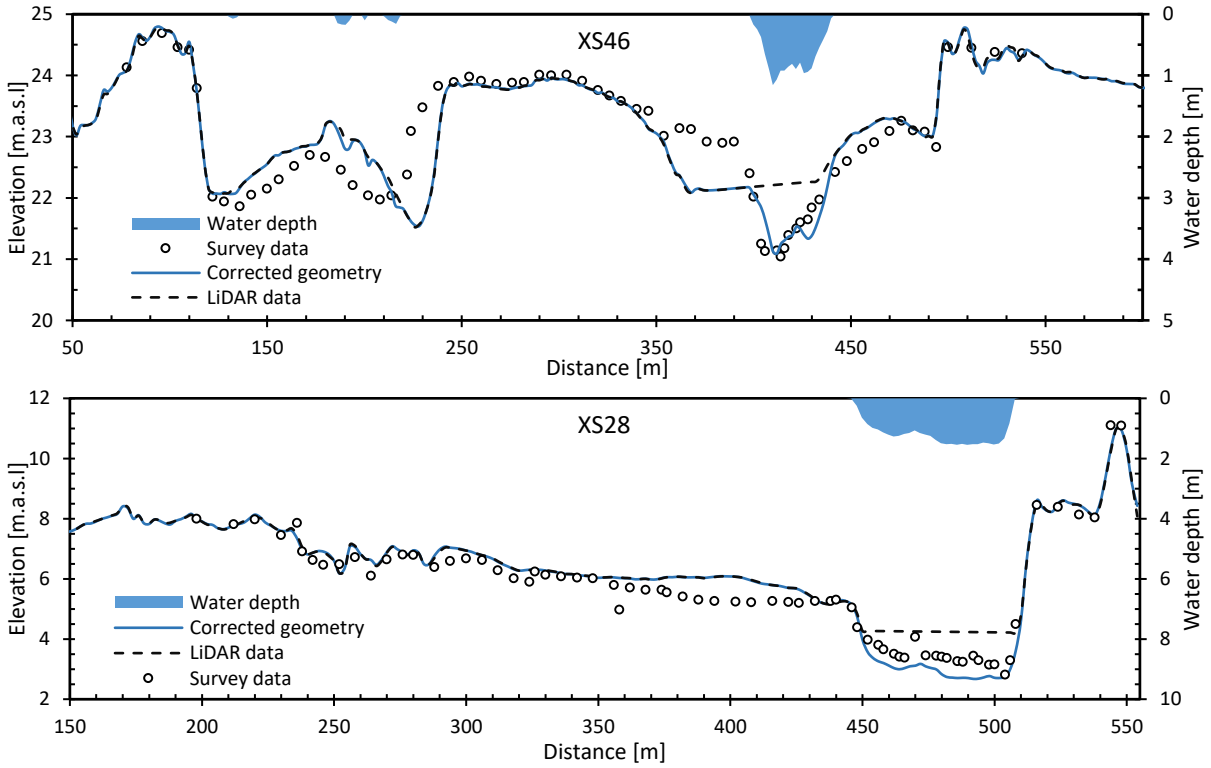


Figure 6 Geometry before and after depth mapping correction

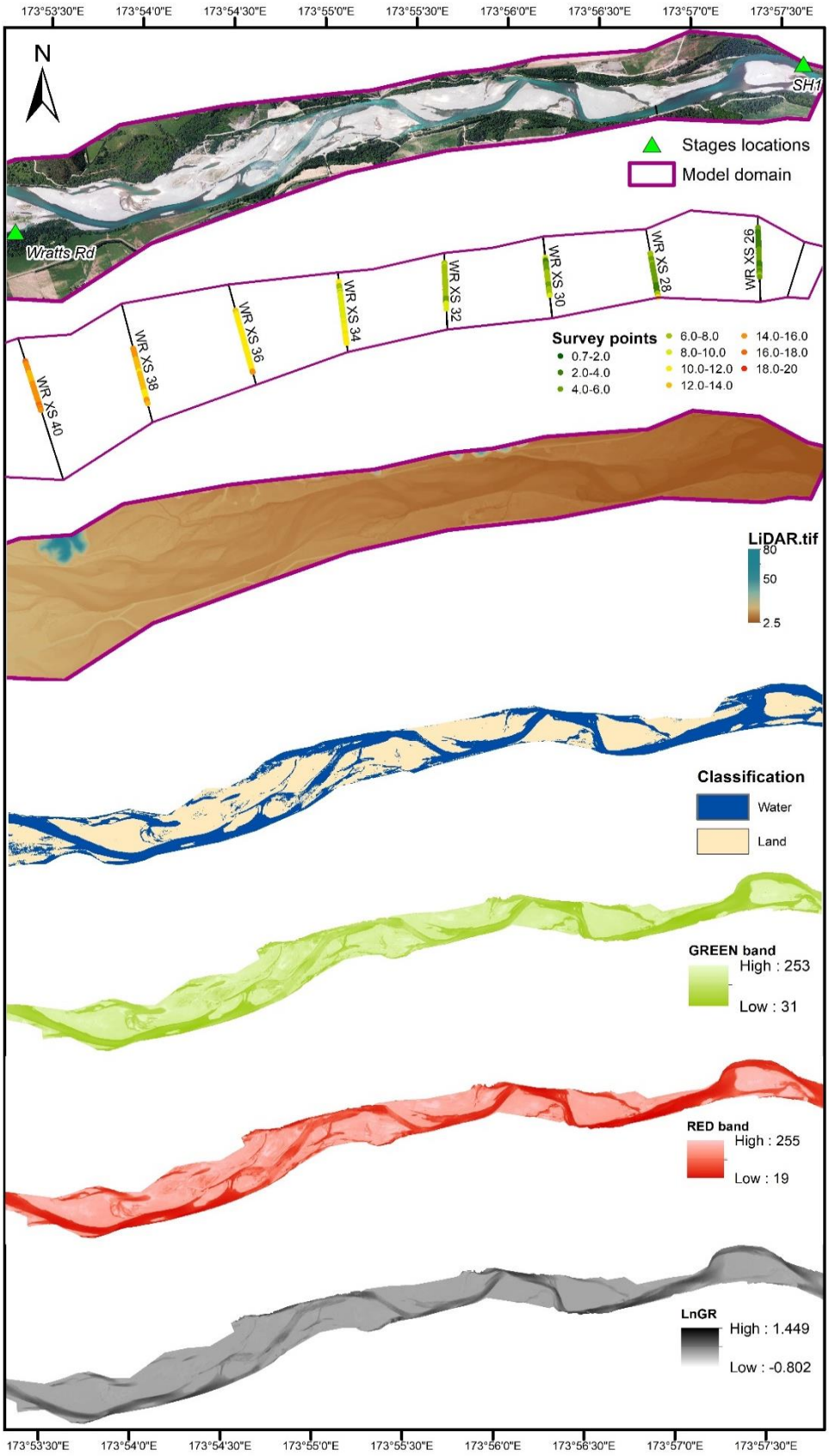


Figure 7 the different layers used for depth calculation

## 3.4 Hydraulic Modelling approach

The study's main emphasis is on the relationship between the geometrical properties of the braided river in different flow conditions. Effects of sediment transport and channel reform after major flood events are not included in the scope, although it is a key descriptor of braided river morphology. Herein the aim is rather more understanding of the changes occurring in water surface width, depth and mean velocities when the flow is changing, commonly referred to as the hydraulic geometry (HG) (Leopold and Maddock, 1953). To that end, a 2D quasi-unsteady state simulation was carried out for different flow values and the hydraulic geometry relations were observed along the study area. The discharge values chosen are 12, 60, 100, 250 and 1000 $m^3/s$ corresponding to the mean annual low flow, median flow, mean flow, and two other medium and high flood events respectively. This range cover flow conditions of in-banks flow, bank-full flow and overbanks flow. While at the same time not reaching high flow values at which significant sediment transport and/or geometry reform is expected (i.e. the average annual flood flow is 1800 $m^3/s$).

The hydraulic geometry relations are simple power functions as follows:

$$w = aQ^b \tag{4}$$

$$d = cQ^f \tag{5}$$

$$v = kQ^m \tag{6}$$

Where $Q$ is the discharge, $w$ is water surface width, $d$ is the mean depth, $v$ and is the mean velocity. $b, f, m$ are the equation exponents while $a, c, k$ are equation coefficients. Because the width, depth and velocity are all functions of discharge, they are all related be the following continuity equations:

$$b + f + m = 1 \tag{7}$$

$$a * c * k = 1 \tag{8}$$

These hydraulic geometry relations where calculated at the three stages locations as well as for the reaches between each two cross section. For each reach, the mean depth and velocity were readily extracted from the spatially distributed results, while the mean water surface width was calculated as the inundated surface area divided by the thalweg length in the considered reach.

The frequency distributions for the simulated velocities and depths were also obtained for all discharge values. In addition, the branch-channel ratio, defined ratio of the sum of all braid lengths over the main channel length, was extracted for every reach as well as for. The Sinuosity index, defined as the ratio of the main channel length to the straight length between its end points was extracted per reach as well.

### 3.4.1 HEC-RAS 2D

The modelling software used in this study is the publically available HEC-RAS, which can use both the Shallow Water (SW) equations and the Diffusive Wave Approximation of the Shallow Water (DSW) equations. In addition to its user-friendly graphical interface, it has other favorable capabilities relevant to this case. A sub-grid bathymetry approach is particularly useful in improving computational time. The approach uses the higher resolution geometry data to create hydraulic tables for every cell of the lower resolution computational mesh (Casulli, 2009), which facilitates the use of a coarser computational mesh. In simpler words, the individual grid cell can be partially wet. Unlike several soft

wares, the cell does not contain only one elevation value, but rather has an elevation vs. storage relationship, derived from the geometry within the cell. Another useful capability to reduce computational time is using the variable time-step option. The user can define a value for Courant number (i.e. the residence time within a cell) and the time step changes accordingly to meet the predefined Courant condition. That means the calculation time step decreases or increases automatically in areas of fast or slow velocities respectively, leading to faster calculations and improved model stability.

HEC-RAS has yet another new added ability that was very useful in the study case. It allows the introduction of internal boundary conditions inside the channel. This feature was used to account for the groundwater-river interaction. A steady inflow/outflow was introduced along the thalweg line to simulate the losses to/ gains from the aquifer. Below are the main steps followed in the model setup.

### 3.4.2 Setup of the computational mesh

The meshing procedure is of high importance in spatially distributed models. Accuracy and temporal resolution of the model output depends on the type and resolution of the mesh. Therefore, the following measures were considered in creating the computational mesh. Firstly, the mesh section along the main river channel was aligned parallel to the streamlines. According to Gallant and Basso (2013), the equations in such flow-oriented mesh are one-dimensional (i.e. the flow progress in one dimension forward), which significantly simplifies the numerical methods. However practically this can be applied for one channel only of the braided river. In this case, the thalweg is considered as the centerline and used to select the main river channel, as suggested by *Merwade et al.,* (2005). The thalweg itself (i.e. the line of lowest heights within a channel) was extracted from the produced depth map by following the highest depth along the river and crossing the lowest point in every survey cross section (Fig.8). Buffering the thalweg gives streamlines and all these lines were introduced to the mesh as break-lines to force the alignment of the mesh line parallel to flow.

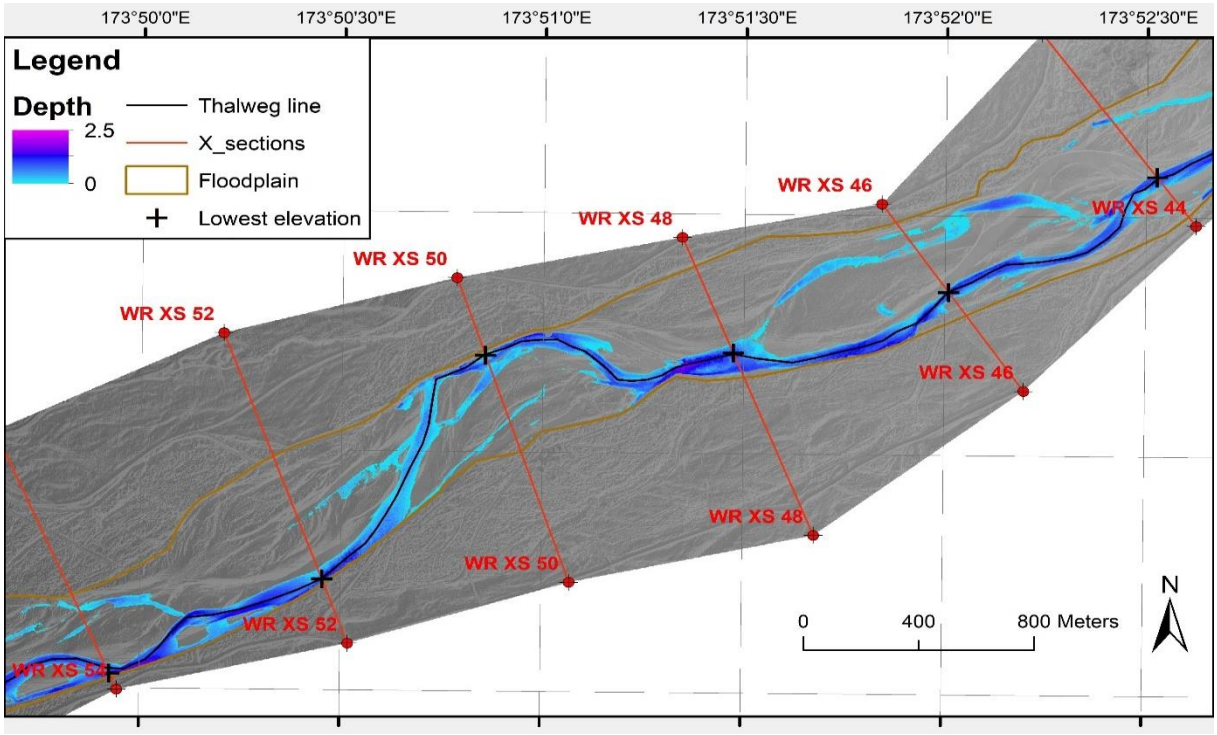


Figure 8 extraction of the thalweg line

Secondly, since the extent of the study is relatively large, an adaptive mesh is used instead of a uniform size mesh. The mesh has two main regions, a refined region of 5*5 $m^2$ cell size in the active flood plain and a coarser 50*50 $m^2$ cell size in the rest of the area. In addition to a transitional area with varying cell sizes along the regions' borders. Furthermore, a hexagonal cell shape was adopted which is found more suitable to the braided nature of the river. It provides better modelling for changes in flow direction since it has a higher chance that the flow is perpendicular to one of the cell faces (CivilGEO, 2019). The resultant computational mesh contains 37 K cell and is shown in figure (9) below for part of the middle river reach. The Refined region boarders are represented by the red break-lines while the thalweg is represented by the blue break-line.

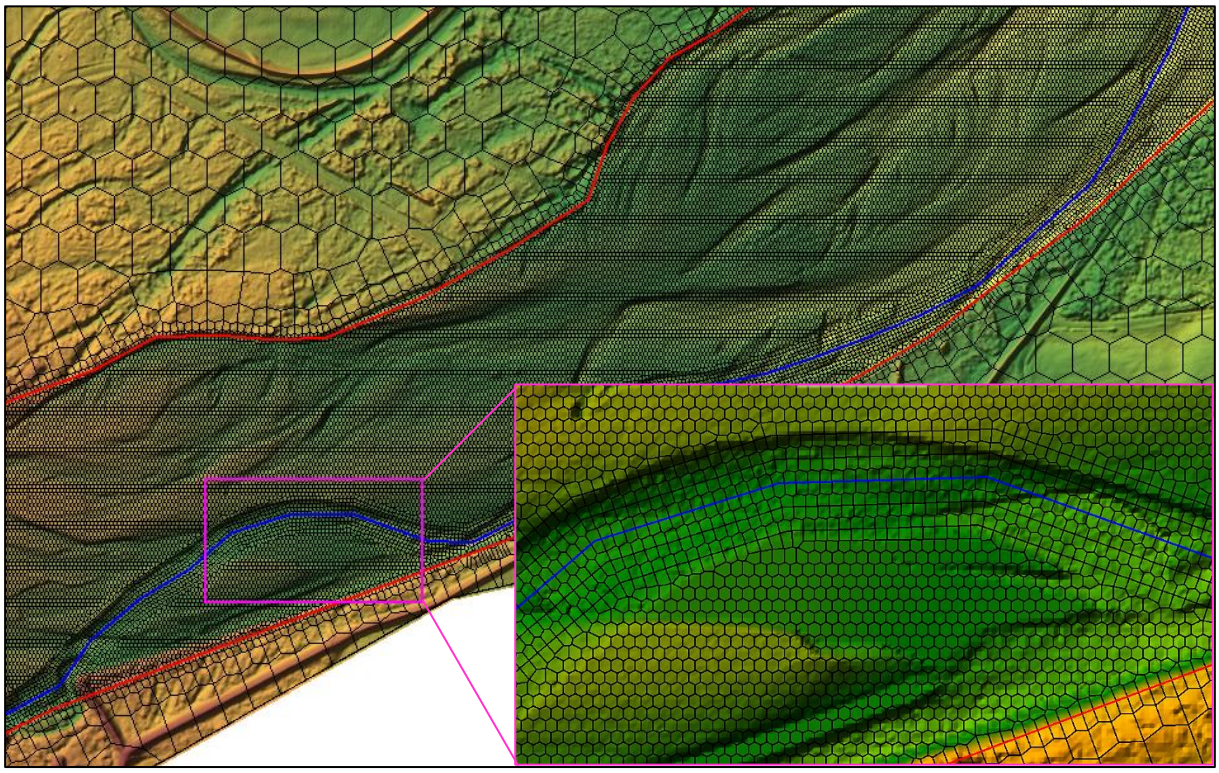

Figure 9 the computational mesh

### 3.4.3 Boundary conditions setup

Different options for upstream, downstream and internal boundary conditions are available including flow and stage hydrographs, rating curves, elevation controlled structures and normal depth. The most suitable option was chosen for each case depending on the type of input data available and the degree of its measurement errors. At the upstream end, the stage hydrograph data were not used due to its sensitivity to height errors, especially given that the augmented DEM contains inherited datum errors as well as errors from the image depth mapping. The flow hydrograph was used instead as upstream boundary condition at Rock Ferry station. For calibration and validation, a 15-mins flow hydrograph data of selected dates were used as input. While for the simulation, a quasi-unsteady flow hydrograph with the predefined discharges is used (fig.10).

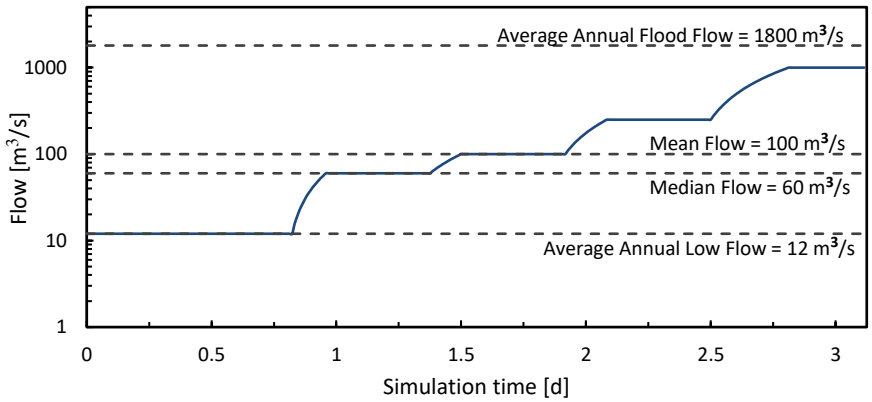


Figure 10 the upstream boundary condition hydrograph

The downstream boundary at Barnet's Bank (SH1) station has both 15-mins stage and discharge data, but when plotting the concurrent readings it is evident that it has multiple rating curves because of the channel movement after major floods. On the other hand, the surface water slope can be extracted from the LiDAR layer and thus providing accurate friction slope to be used in the normal depth method. However, the flow readings at SH1 were still used in calibration.

To account for groundwater interaction, the river was split into three reaches between the four gauging stations. Then a water balance was carried out for a period of one day to measure the volumes passing through each gauging station. For accurate water balance, the flow lag time was measured between stations by means of simple time series analysis (fig.11). The difference in water volumes between each two stations - in the absence of small stream inflows - represent the groundwater losses or gains in that reach. These volumes were then converted to steady flows and introduced in each reach as internal boundary conditions using the thalweg line. It worth mentioning that the groundwater interaction was considered only in the calibration and validation step as it requires a real time series. In the simulation however, no groundwater interaction assumed. This is in part due to the uncertainty associated to high flows estimation, but it also provides an opportunity to use the model output in groundwater estimation (specifically in perched conditions).

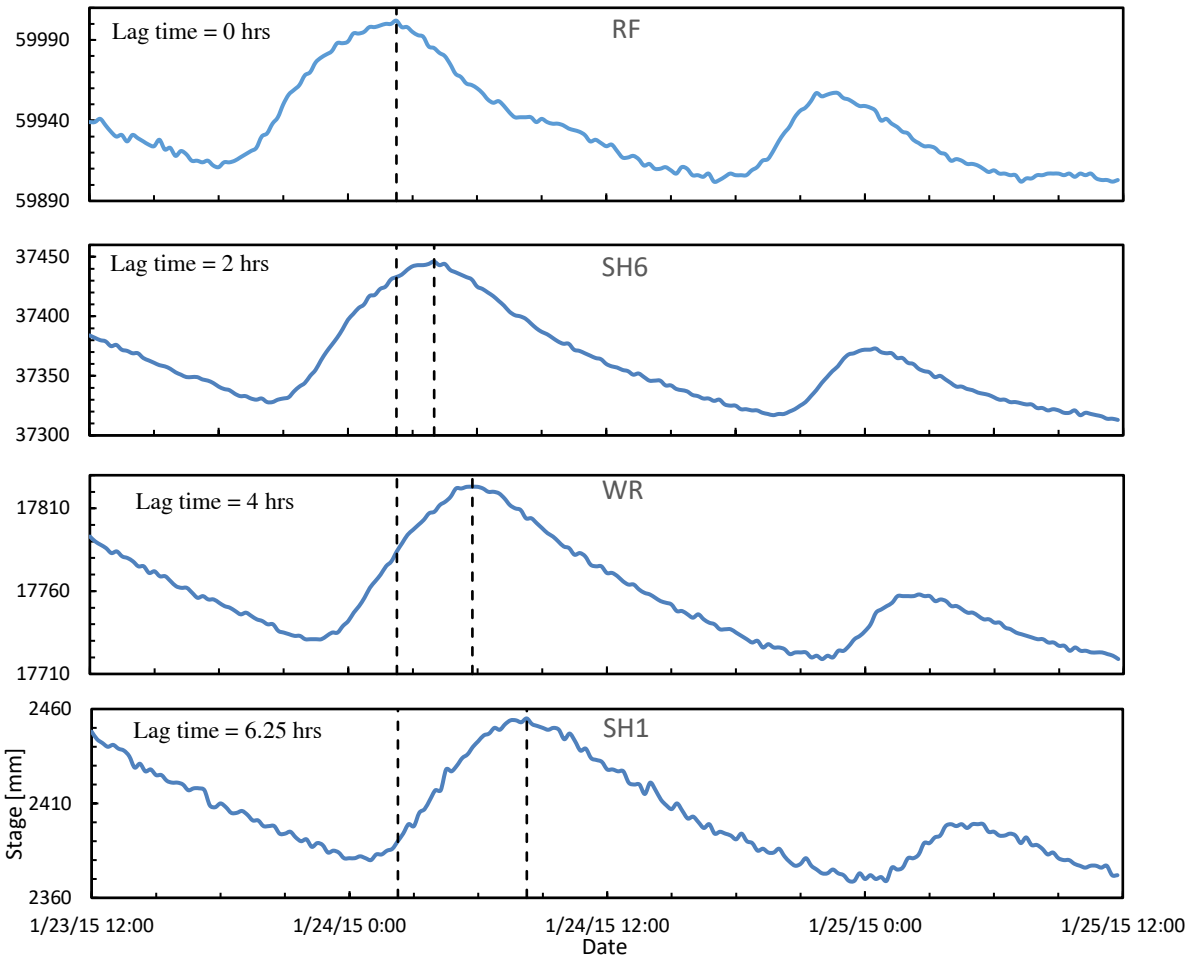


Figure 11 flow lag time between the stage locations

### 3.4.4 Calibration and validation

Braided rivers are generally described by low flow depths and slopes, which means that the riverbed friction plays a major role in controlling the flow. Therefore, the main parameter considered for calibration is the Manning coefficient. The model assumes a homogeneous gravel bed in the active flood plain thus a lumped parameter value. A trial-and-error approach was adopted by changing Manning value and comparing the output hydraulic properties with the measured data. However, comparing the water level downstream at SH1 proved difficult because of discrepancies between the LiDAR's datum and that of the stage. Another approach is to compare the inundated areas from the model and aerial photos but it was also discarded. Because of the changing nature of the riverbed, different inundated areas maps can result from the same discharge without necessarily change in the friction.

That leaves us with comparing the flow velocity, which is –according to Manning's equation- directly affected by friction. In this approach, a peak of $Q_{max}$ value was traced along the river and its time of arrival was registered at the three stations downstream. The Manning value that gives the least difference in arrival times between the observed and simulated data at the three stations was adopted. For validation, the performance predictors of a second hydrograph with the same range of $Q_{max}$ were checked (namely; NSE, KGE and Bias). This method produced good results -especially in low and median discharges- considering the high temporal resolution of the hydrograph and the relatively long river reach (23.5 Km).

According to several studies however, Manning's value changes with discharge (Arcement Jr. and Schneider, 1989; Williams *et al.*, 2013). A study by Kim *et al.* (2010) in a gravel-bed river shows that the Manning's coefficient decreases with increasing discharge, until reaching a threshold value after which it stays constant. Therefore, the calibration was carried out for two low and median range discharge values and the change in Manning's value was observed. For discharges more than 100 $m^3/s$ the uncertainty in rating curve readings – especially at Wratts Rd station- becomes unsuitable for fine-tuning Manning's value. Further computational options are outlined in table (1) below.

Table 1: Computational options for the modelling setup

| Option | Value |
|---|---|
| Equation set | Diffusion wave |
| Input/output interval | 15 min. |
| Flow tolerance | 0.1 % |
| Surface water tolerance | 0.01 m |
| Calculation time step | Variable based on Courant condition |
| Maximum Courant number | 2.0 |
| Minimum Courant number | 0.5 |

# 4 Results and Discussion

## 4.1 Augmented Geometry

### 4.1.1 Height error correction

Firstly, the systematic height difference between LiDAR and Survey data was found to be 0.39+/-0.02 m (Mean +/- SEM). It is calculated from a sample of 1,519 Survey points in total on the dry areas. The scatter of the sample, 0.81 m, can be attributed to the change in flood plain geometry accrued between 2012 and 2014. Figure (12) shows the boxplot and frequency distribution of the height difference ($Z_L - Z_S$). It is evident that the LiDAR data gives higher values than the Survey data for the same point. The 25-75 percentiles are 0.15/0.77 m respectively and the whiskers represent the 5-95 percentiles, which are around -1.0/1.5 m. All outlier points outside the whiskers were checked visually form the aerial photos. They are either located on a high vegetation cover or at a location of step change in height which was shifted between the time of survey and LiDAR data. On the other hand, the few points that were located on embankments or roads corresponds well to the mean and median error values around the 0.39 m mark. This height difference value is the added to all survey points as a correction before calculating the survey depth from eq. (1). However, this implies a difference in the datum between the two datasets, hence affected the reliability of height values, which in turn affected the choice of calibration method.

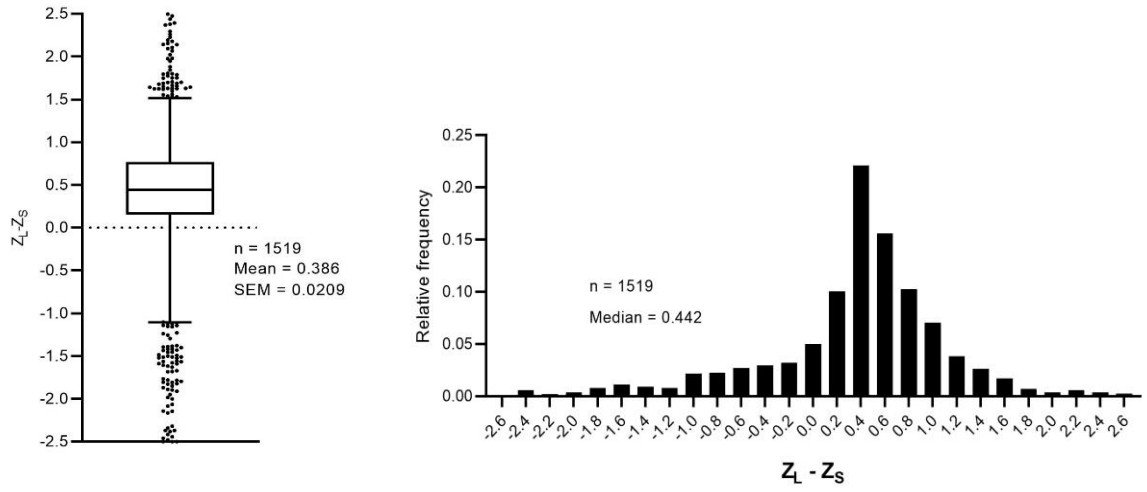


Figure 12 Box plot and distribution frequency of height difference

### 4.1.2 Color-depth relationship

Secondly, for the depth-colour relationship, the regression analysis on the calibration dataset yielded good correlation ($R^2$= 0.657) with a standard error of predicted depth $\sigma_d$ = 0.257m which accounts to 30% of the mean sample depth (Fig. 13a). This depth retrieval error is relatively small in comparison to the validation sample size (n = 80) and it is further improved when considering the whole sample size (140) shown in figure (13b). To test depth retrieval accuracy, the image-derived depths were plotted vs survey depths for the validation dataset sample. The line slope shows small departure from the 45° angle

and positive intercept value (Fig. 13c). That indicates a tendency to overestimate depths less than 1.0 m and underestimation for higher ones. However, the sample points with depths > 1.0 m are few in number and are not homogenously distributed in all cross sections to support the underestimation tendency.

On the other hand, it worth mentioning that such bias is considered as fundamental limitation of this method. Legleiter *et al.*, (2004; 2013) relates this underestimation tendency in deep pools to the limitation of the radiometric resolution of the photo. He argues that since the bands have values between 0 and 225 to describe all surfaces on land and water, it leaves only small portion of unique values to correlate to different depths. Nevertheless, from analysing the histogram of the red and green bands over water, it is evident that this was not the case in this study. The range of unique values is between 45 – 130 in the Red band and between 85 – 189 in the Green band, in contrast to only 28 unique values in the study by Legleiter *et al.*, (2013). This is achieved by the high spatial resolution of the Aerial photo of 0.4*0.4 $m^2$.

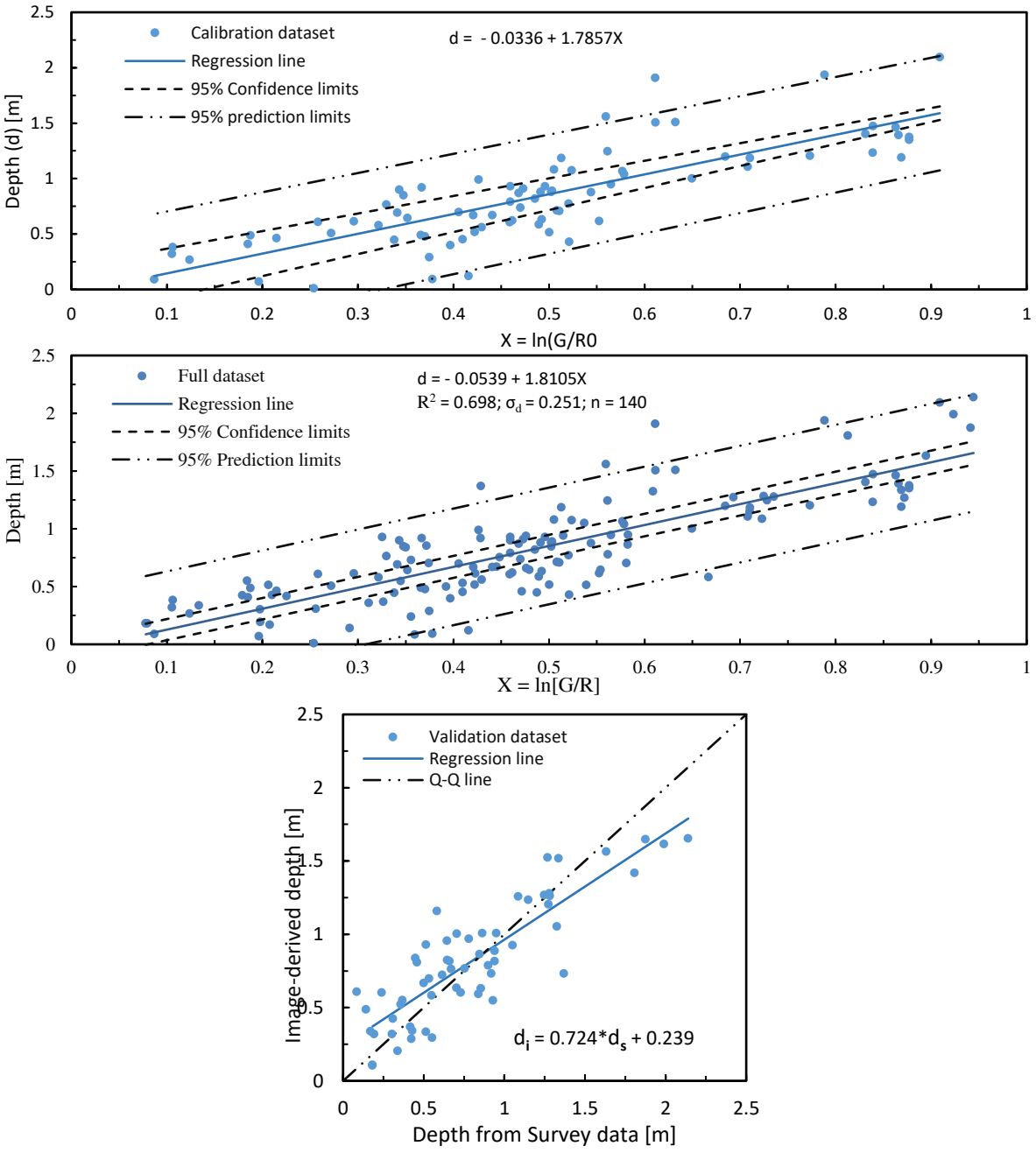


Figure 13 color-depth relation for (a) calibration dataset, (b) complete dataset, and (c) depth retrieval accuracy

### 4.1.3 Depth layer and final geometry

By applying the equation above on all water pixels, we get the water depth map shown in figure (15a). The depth ranges from 0.01 to 2.55 m with an average of 0.57 m and covers an area of 2.31$Km^2$. Subtracting this depth from the LiDAR layer adds another 1.325 MCM to the geometry, which was submerged by water. For the considered reach in the study area (23.5 km) and using the average depth, this volume corresponds to an average channel width of 98.9 m. Overall, these statistics agrees well with the measured depth and width from both survey data and aerial photos. However, the depth layer contains additional errors not related to the depth retrieval equation above. These non-systematic errors are found in areas where a vegetation cover or shadow overcasts the water surface. Figure (14) shows an example where the bridge and the vegetation on the left bank side covers part of the water surface as well as a small tributary channel. In this case, only the depth for the visible part can be calculated and the resultant geometry will have an abrupt change in height on that edge. Moreover, the shadow from SH6 Bridge also leads to depth overestimation at this location due to the darker colour. Nevertheless, these unsystematic errors are relatively few when considering the whole study area. For the most part, the water surface is exposed with no vegetation covering the banks.

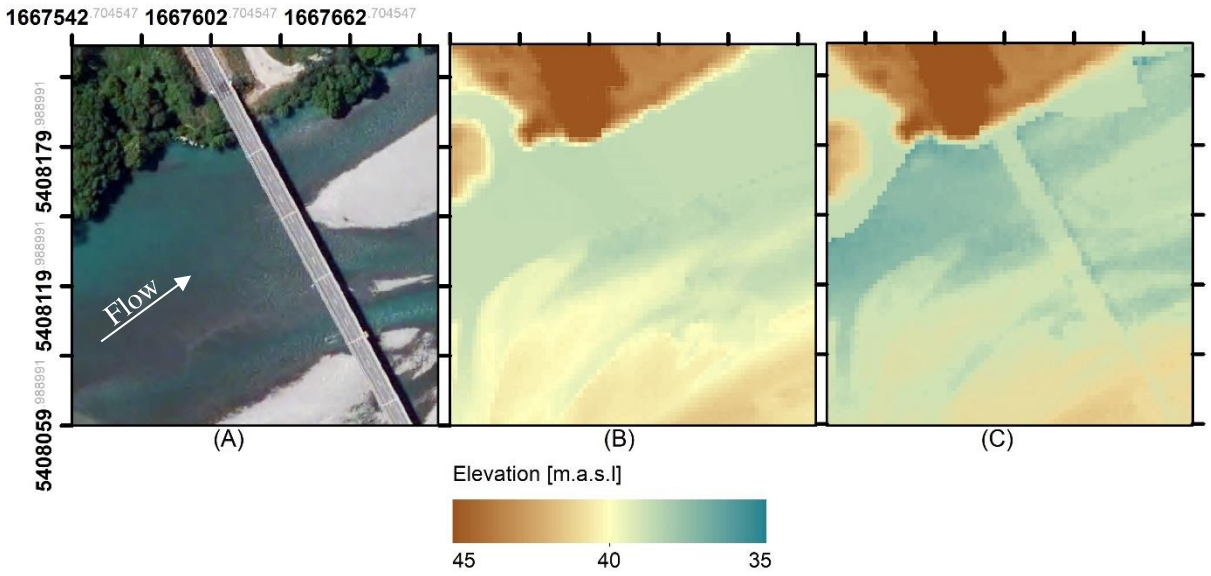


Figure 14 Geometry errors on covered water surface

The final augmented geometry covers the whole flood plain area with an overall height accuracy of +/- 0.06 m in dry areas and +/-0.206 m in the inundated areas figure (15b).

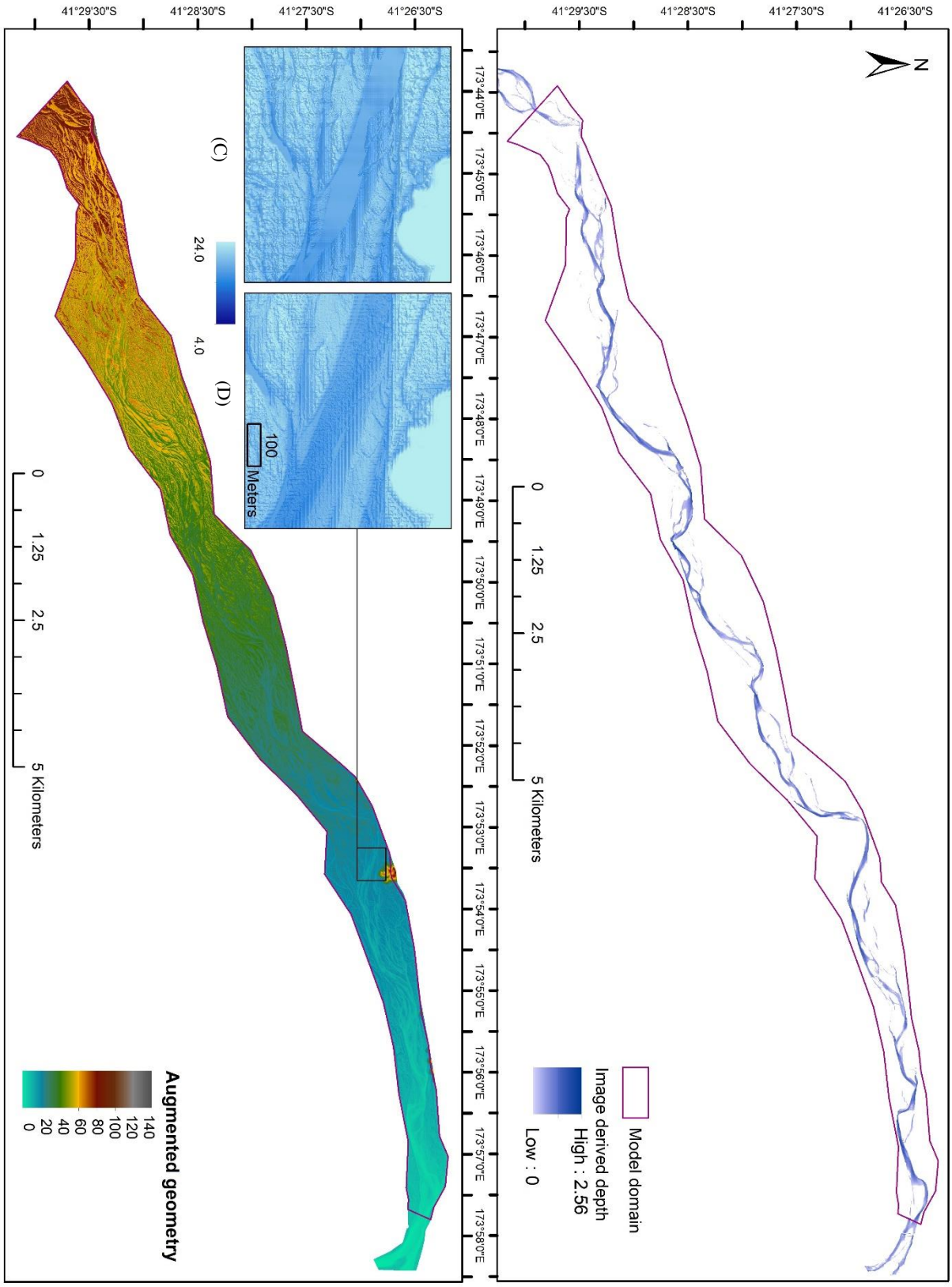


Figure 15 (a) Image derived depth layer and (b) the adjusted geometry (C) before and (D) after depth subtraction

## 4.2 Hydraulic simulation results

### 4.2.1 Model calibration and validation

The calibration for roughness parameter was carried out at both low flow and median flow conditions separately. Figures (16, 17) below shows the different simulated and observed time series in calibration step (left hand side) and validation step (right hand side). The Optimum Manning's value at low flow was found to be 0.035 with highest $R^2$ and NSE at 0.985 and 0.883 respectively. As for median flow conditions, the optimum Manning's value decreased to 0.030 with $R^2$ equals 0.913 and NSE equals 0.851. The validation time series in both cases gave $R^2$ values in the same range and KGE values for all runs was higher than 0.65. Table (2) summaries the goodness of fit test values for all mentioned simulation runs.

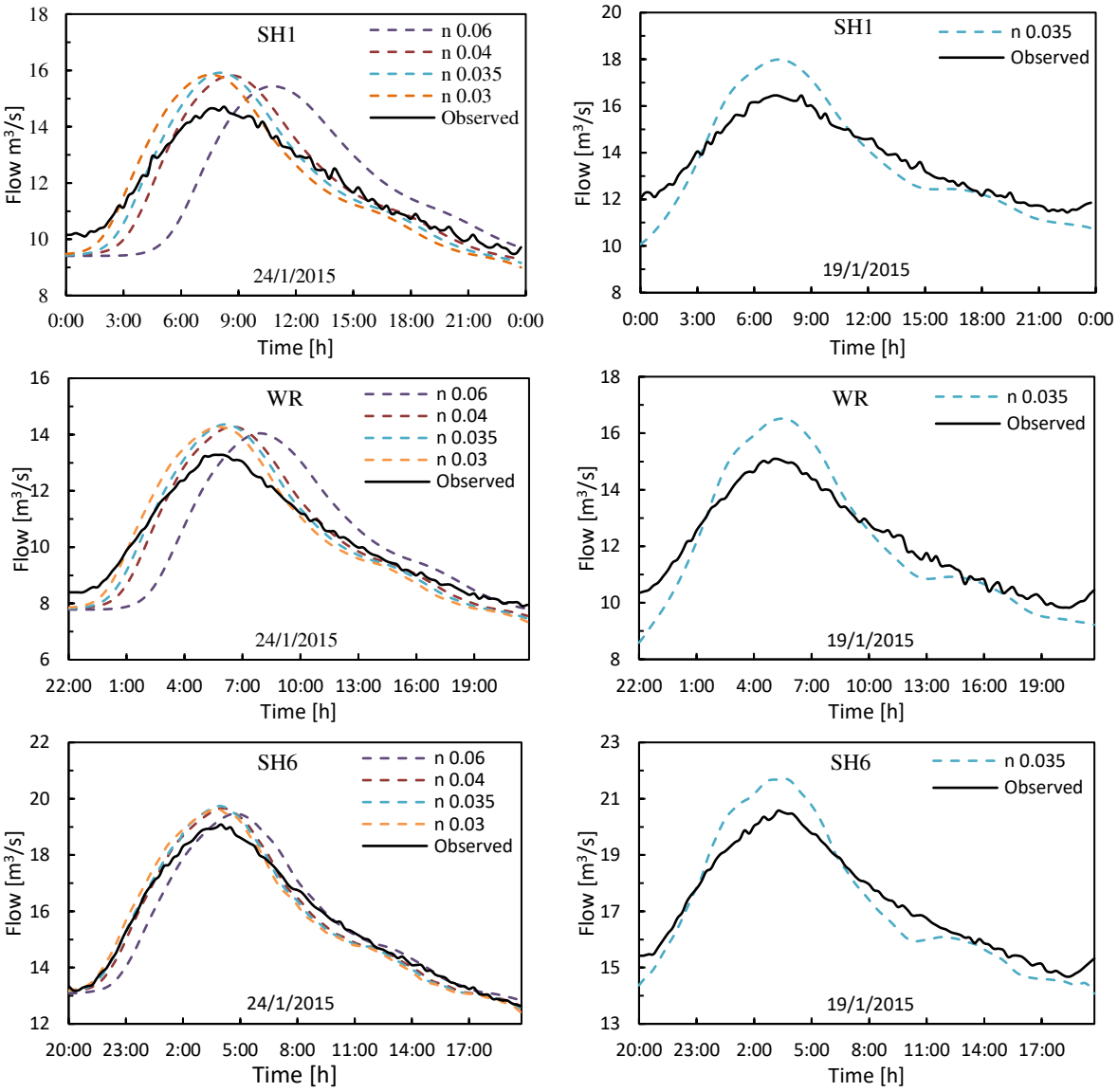


Figure 16 Simulated vs observed time series in calibration step (left side) and validation step (right side), Low flow condition

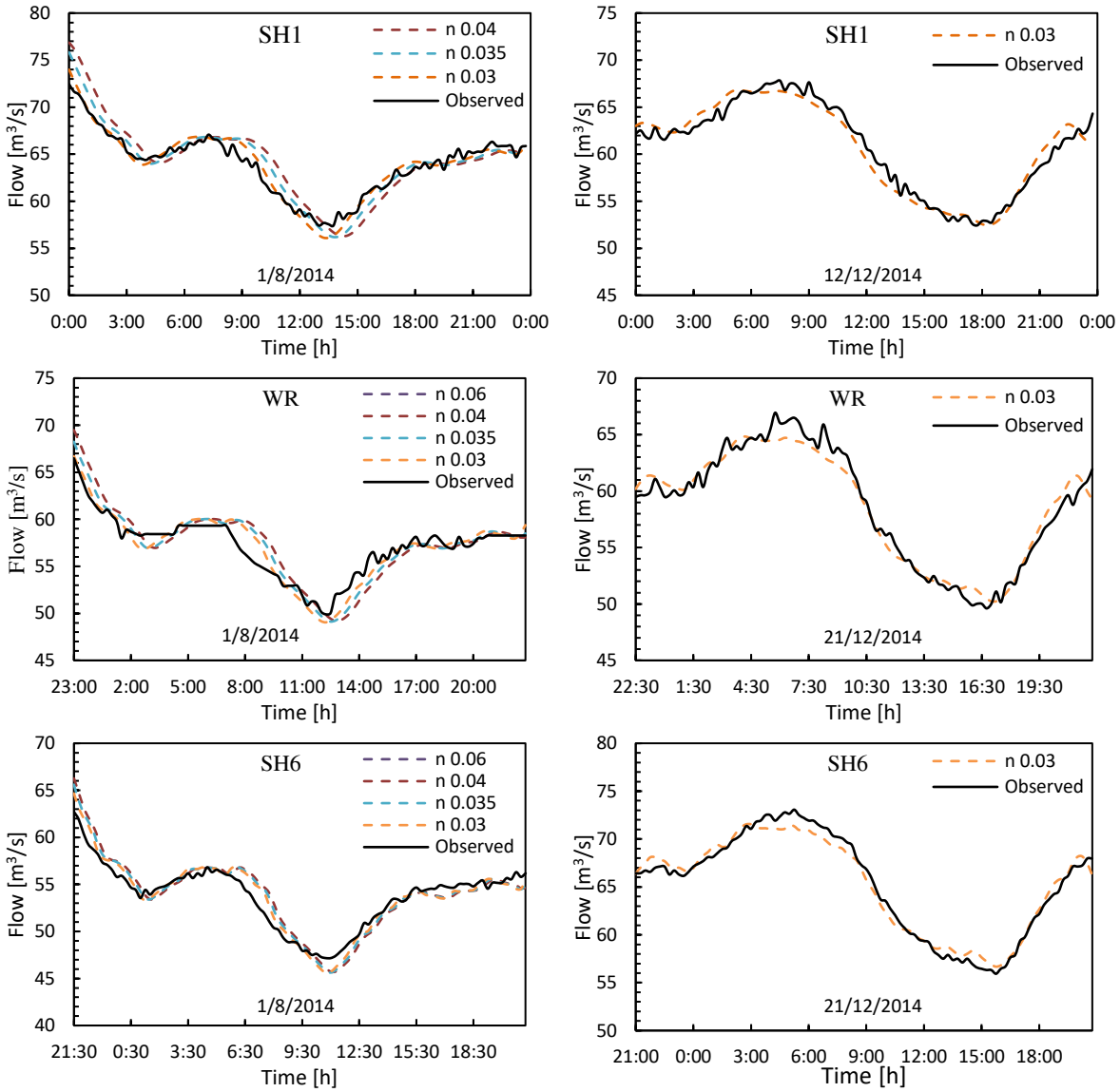


Figure 17 Simulated vs observed time series in calibration step (left side) and validation step (right side), Median flow condition.

A study by Kim *et al.* (2010) found that the roughness coefficient decreases with increasing discharge in gravel bed rivers, and remains constant after certain discharge. This is mainly attributed to the fact that in low flows the cross-sectional area/wetted perimeter ratio is relatively smaller than in high flows. It is more evident in braided rivers with wide active flood plains than in single U-shaped channel rivers. Moreover, the meandering of the river at low flow conditions attributes to increasing the roughness value (Arcement Jr. and Schneider, 1989). Meanders alone can increase the Manning's value up to 30% (Chow, 1959). On the other hand, spatial variability of the roughness coefficient plays an inverse role. The riverbanks and sand bars have rougher surface than the riverbed. Although the surface materials of both are homogeneous, small vegetation cover grows on the sand bars in low flow conditions. Therefore when submerged at high flows they tend to increase the overall roughness coefficient of the river. Based on all the previous, the Manning's value at median flow conditions (i.e. n = 0.03) was selected as the base value and used on the simulation. It is assumed to stay constant for higher flow values due to the balancing effect between increased banks roughness versus reduced hydraulic radius and meandering. At the same time, n = 0.03 still scored $R^2$ and NSE values that are very close to the optimum value at low flow.

Table 2 Performance metrics for the different simulations in calibration and validation

| | | date | $Q_{max}$ [m³/s] | $Q_{min}$ [m³/s] | $Q_{mean}$ [m³/s] | Manning's value 0.060 | 0.040 | 0.035 | 0.030 |
|---|---|---|---|---|---|---|---|---|---|
| low flow condition | calibration | 24/1/2015 | 14.71 | 9.5 | 11.89 | NSE 0.363<br>$R^2$ 0.6<br>KGE 0.673 | NSE 0.868<br>$R^2$ 0.963<br>KGE 0.725 | NSE 0.883<br>$R^2$ 0.985<br>KGE 0.71 | NSE 0.858<br>$R^2$ 0.965<br>KGE 0.701 |
| | validation | 19/1/2015 | 16.44 | 11.44 | 13.69 | | | NSE 0.85<br>$R^2$ 0.97<br>KGE 0.67 | |
| median flow condition | calibration | 1/8/2014 | 72.46 | 57.41 | 63.95 | | NSE 0.73<br>$R^2$ 0.856<br>KGE 0.72 | NSE 0.851<br>$R^2$ 0.913<br>KGE 0.803 | NSE 0.922<br>$R^2$ 0.945<br>KGE 0.873 |
| | validation | 21/12/2014 | 67.82 | 52.43 | 60.73 | | | | NSE 0.957<br>$R^2$ 0.958<br>KGE 0.953 |

### 4.2.2 Branching and sinuosity of the river

The thalweg line was used as the river centerline to calculate both the Sinousity Index (SI) and the Braid-Channel Ratio (Br). SI was found to be 1.185 for the total reach length. By further deviding the study area into Upper, Middle and Lower reaches between the stages locations, the Sinousity was determined for every reach individually. The middle reach (SH6 to WR) undergoes the heighest Sinousity at SI = 1.20 followed by the upper reach (RF to SH6) at 1.16 while the lower reach (WR to SH1) has the smallest SI value at 1.13. The braid-channel ratio on the other hand is discharge dependent. It increases with discharge as more braids are filled with water. Statistical values for Br are shown in table (3) below for all simulated discharges. The initial Braid-channel ratio at low discharge is close to unity for upper and middle reaches, meaning that there are as much branches (in length) as the main channel. It can also be seen that the upper reach registers the highest increase of Br with increasing discharge while the lower reach has the least Br. These Br and SI values indicate that every reach reacts relatively differently to flow. In other words, the upper reach undergoes the most branching, the middle reach undergoes the most meandering while the lower reach undergoes the least of both.

Table 3 The braid-channel ratio for the reaches at different discharges

| Flow [m³/s] | Braid-channel ratio (Br) Overall reach | Upper reach | Middle reach | Lower reach |
|---|---|---|---|---|
| 12 | 0.87 | 0.99 | 1.08 | 0.47 |
| 60 | 1.21 | 1.559 | 1.23 | 0.80 |
| 100 | 1.44 | 1.75 | 1.48 | 1.05 |
| 250 | 1.99 | 2.52 | 1.91 | 1.52 |
| 1000 | 2.58 | 3.47 | 2.34 | 1.92 |

### 4.2.3 Spatial and frequency distribution of simulated hydraulics

Figures ( 18 - 20 ) below illustrates the spatial variability of depth, velocity and water level profile for selected discharges, where the deeper colors represent higher values. At low flows, the main channel is easily identified. As flow increases, new shallower branches apper and the main chanell gains more depth.

The spatial distribution of wetted braids is in close agreement with the Br and SI values. For the upper reach braiding is more evident. Some papers relate this phenomena to a systematic aeffect of the upstream boundary condition (Nicholas, 2003). If the boundary condition is treated as one cross section then the initial flow might be distributed to more branches than actually observed in reality. However, is not the case here since 95% of the flow passes through the main channel and only small part is diverted to a small branch, and they connect only 750 m downstream before branching again. The high braid-channel ratio is attributed instead to being downstream of a conflouence, where channels of different bed elevations and slops run parallel to eachother before converging.

The middle reach on the other hand experience lesser branching and more sinuosity evident by the increased number of bends. In comparison to the upper reach, the braids are shorter in length and closer to the main channel with a slight increase in velocity. As for the lower reach, the braiding intensity drops significantly in favor of higher depth values. The effect of increased floodplain confinement and lower slopes is also evident as some braids are backfilled with water in the opposite direction to flow.

As discharge increases, so does the main channel's depth and velocity, and the new branches reach lengthe, depth and velocity values close to that of the main channel at low flow. In other words, the branches replace the main channel condition while the latter increases in depth and velocity. In a way, this process is equivalent to adding a deeper faster channel to small existing ones. This process might look homogenious for bigger scales, but there are considerable variability in depth, velocity ansd slope values between the individual braids. On a small scale, aprubt changes in hydralics happen at some threshold values of the discharge. The study of frequency distribution of simulated hydraulics in conjuction with spatial distribution help to explain some behaviours.

Depth and velocity values registered along the study reach ranged between 0 -5.06 m and 0 - 5.89 m/s respectively. The mean depth increased from 0.39 m at Q = 12 $m^3$/s to 1.29 m at Q = 1000 $m^3$/s and mean velocity increased from 0.34 m/s to 1.82 m/s for the same discharges. However, mean values doesn't describe simulated varialbility. The histograms in figure (21) below show the frequency distribution for depth (right hand side) and velocity (left hand side) values at all discharges. Firstly for the depth, the histogram is positively skewed to the right in all discharges with the mean depth bigger than the median depth. On average, the median depth accounts to 0.845 of the mean depth. The modal depth on the other hand is found to be much smaller. It accounts for 0.1 and 0.2 of the mean depth at low and median discharges respectively, and 0.05 of mean depth for higher discharges. Such low modal depth is an indicator of the sheet flow depth over sand bars as oppose to channel flow depth, which is expected to be higher. This ferquency distribution gives a good describtion of the river morphology. For rivers with U-shaped or rectangular shaped channels, a negatively skewed histogram is expected as the centeral measures (i.e. mean, median, mode) shift towards higher depth values.

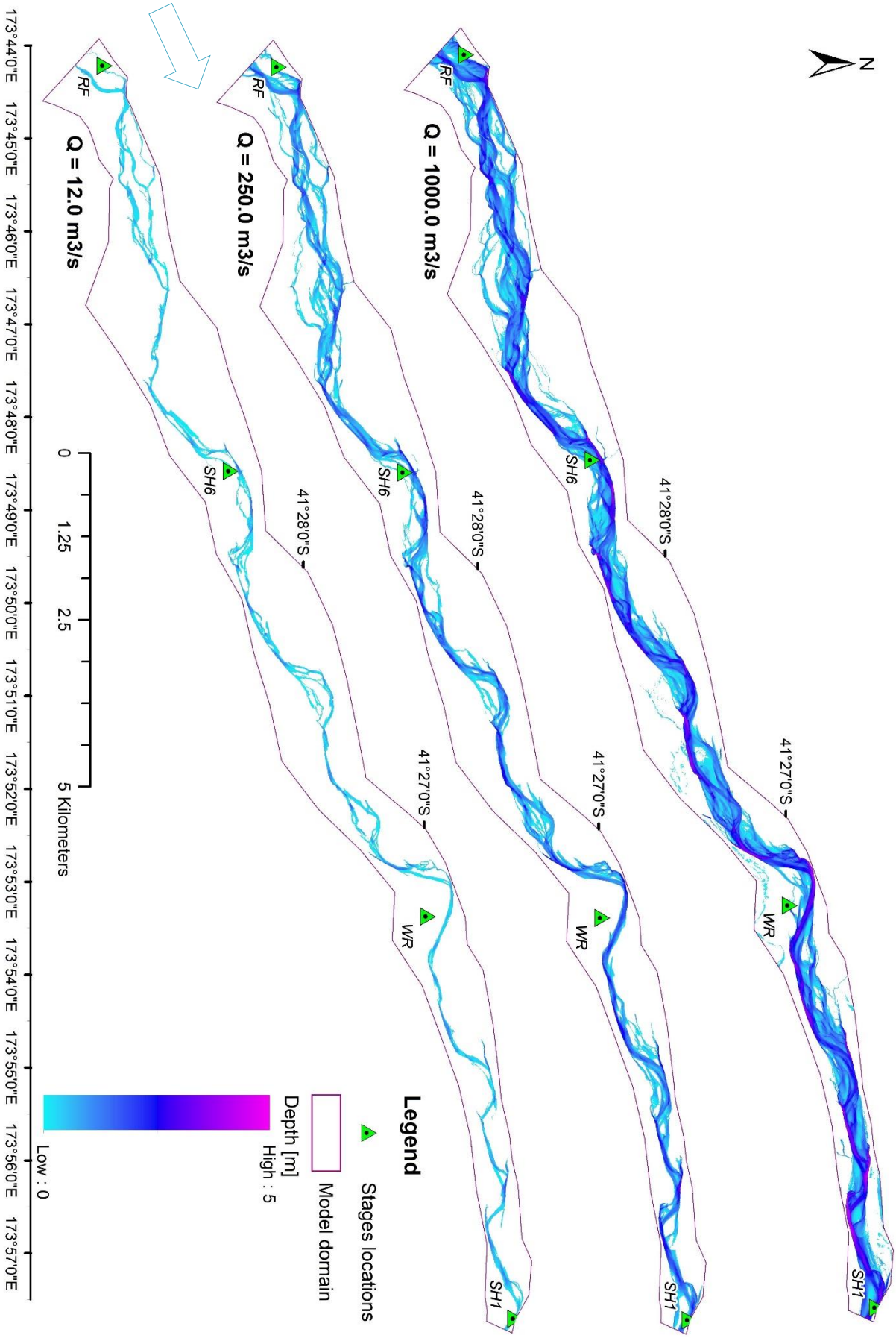


Figure 18 Simulated depth for selected discharges

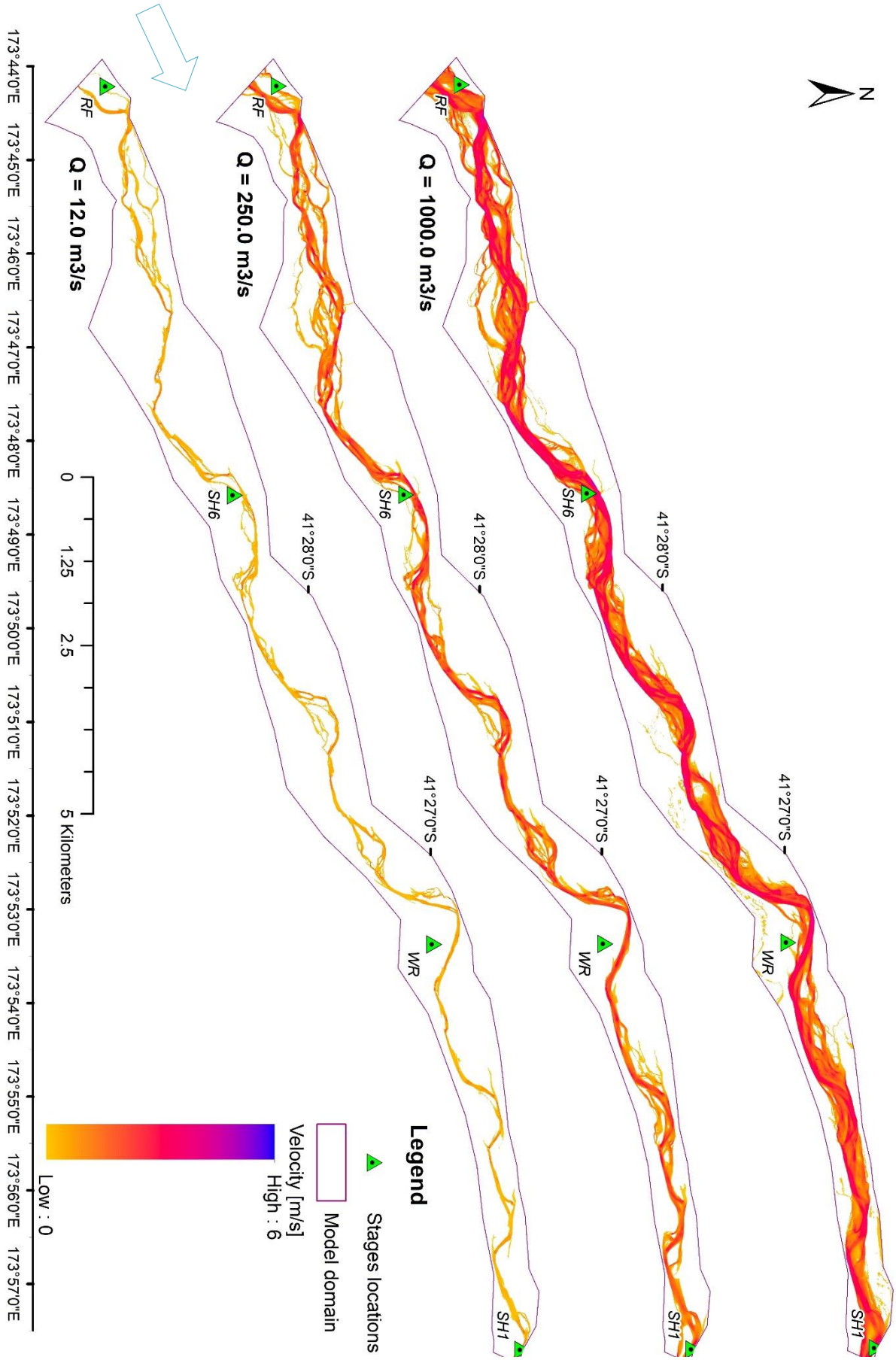


Figure 19 Simulated velocity values at selected discharges

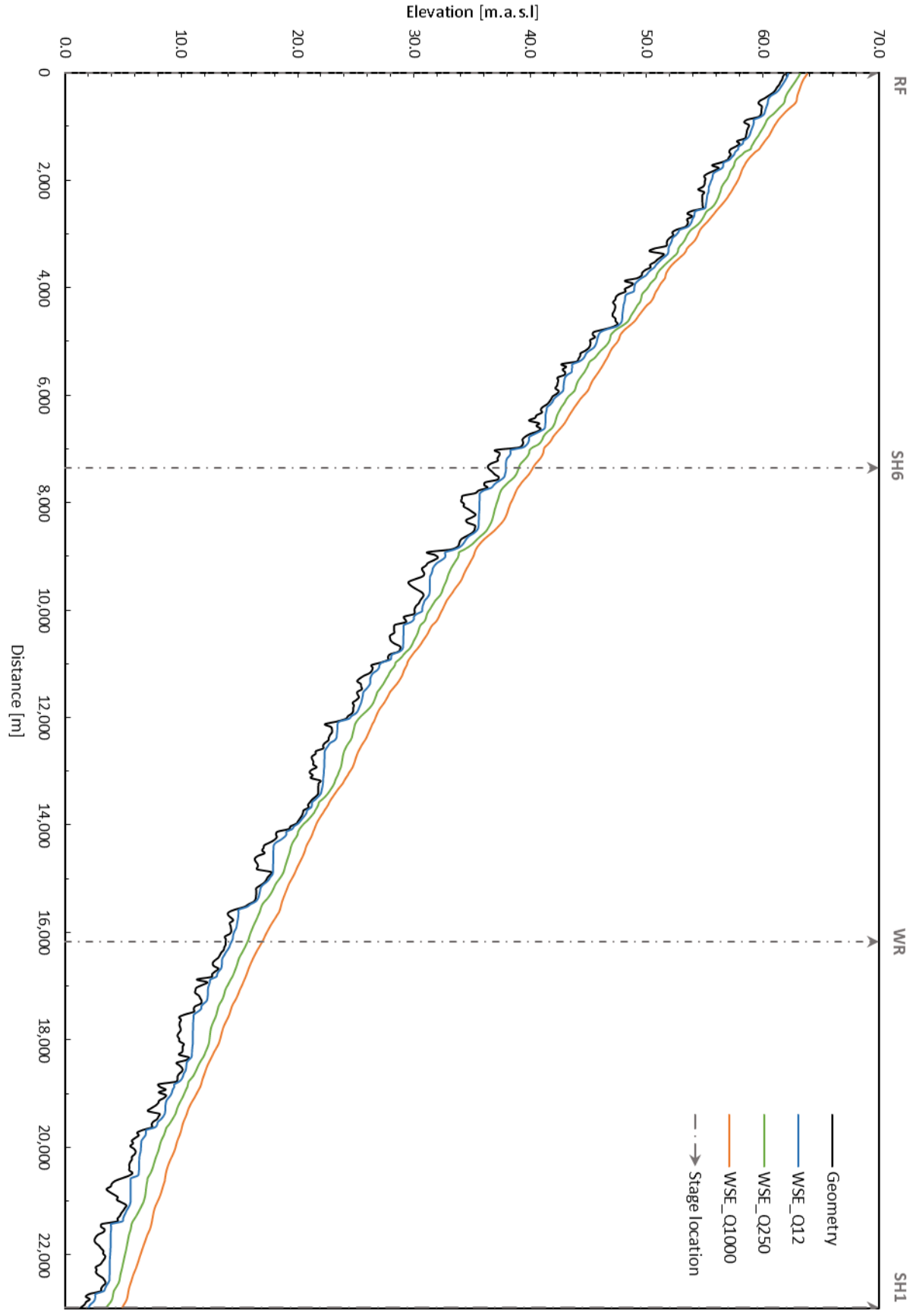


Figure 20 Surface water profiles at selected discharges

Secondly for the velocity values, the frequency distribution changes from positively skewed at low discharge to bi-modal distribution at medium discharges then to edge-peak distribution at high discharges. In contrast to depth frequency, the velocity frequency provides better distinction between sheet flow and channel flow conditions. The lower modal velocity peak (< 0.25 m/s) corresponds to sheet flow and backwater conditions while the higher modal velocity peak corresponds to main channel flow (e.g. 1.25 m/s at Q = 100 $m^3$/s). The median and modal velocities accounts for 0.95 and 0.91 of the mean velocity respectively. A study on 72 reaches of New Zealand rivers by Jowett (1998) Shared these same modal velocity ranges and bi-modal shape. However the reported modal depth was much heigher at around 0.8 of the mean depth.

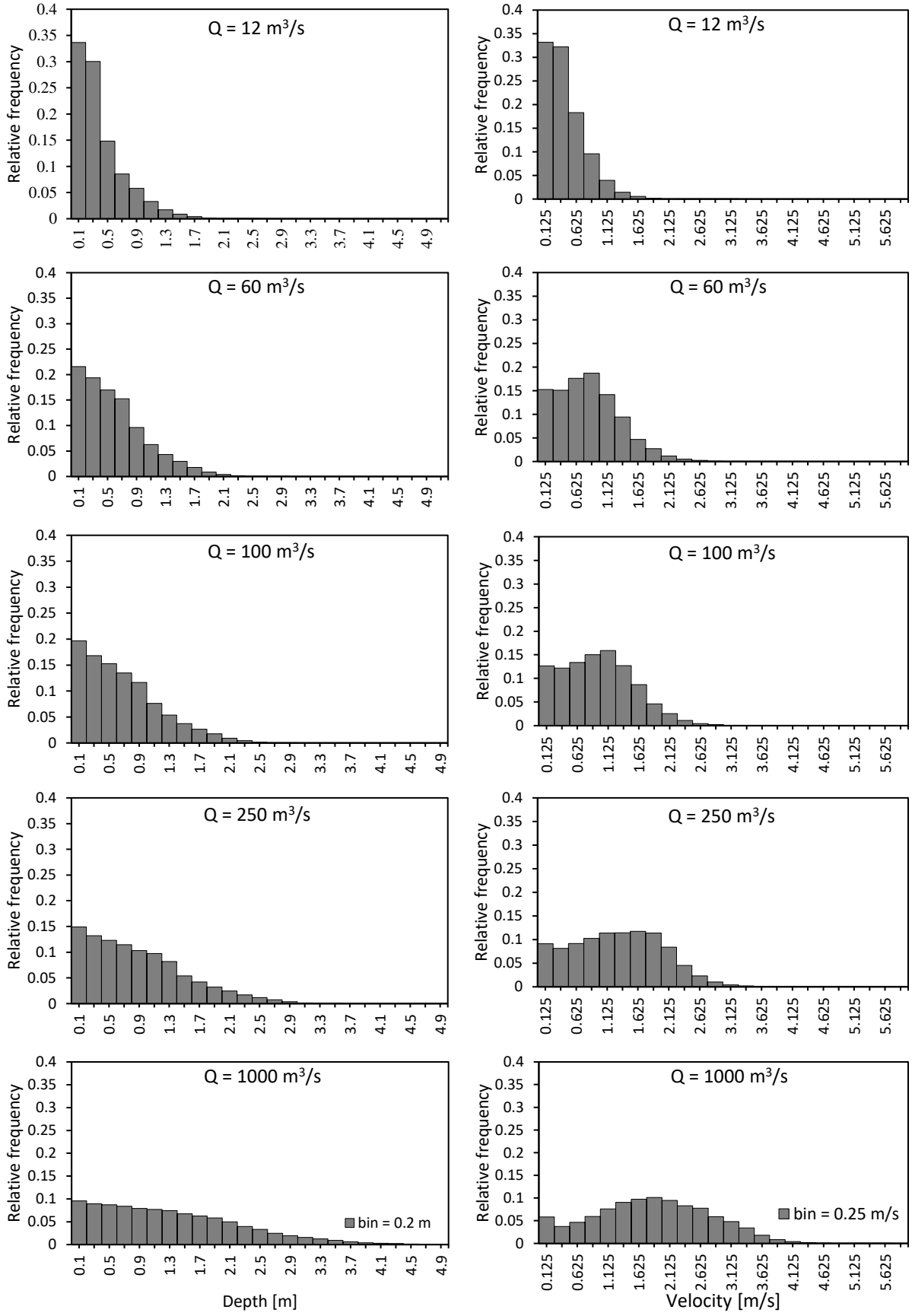


Figure 21 Frequency distributions for simulated depth (left) and velocity (right) at different discharges

### 4.2.4 Channels shape exponent

The shape exponents were calculated for the cross sections at stage locations. Each cross-section is considered to represent the preceded reach upstream since the channel geometry is changing downwards. The shape exponent was found higher for cross section SH6 at 1.13 followed by cross section WR at 0.99 and the lowest was SH1 at 0.88. This decreasing trend corresponds to a decrease in braiding intensity. Figure (22) below shows the three cross sections with water levels at different discharges (left hand side) along with the shape exponent relationship (right hand side). For $b_c > 1.0$ such as in SH6, the reach is considered braided because the rate in increasing channel width with height is high. At this cross section, there are several parallel braids with different bed elevations, so when the water elevation is increased, new braids are wetted and add more water surface width per elevation increment. For $b_c = 1.0$ the width is linearly increasing with depth. This trend is commonly observed in alluvial rivers with unconfined or wide floodplains and represents that of a V-shaped channel.

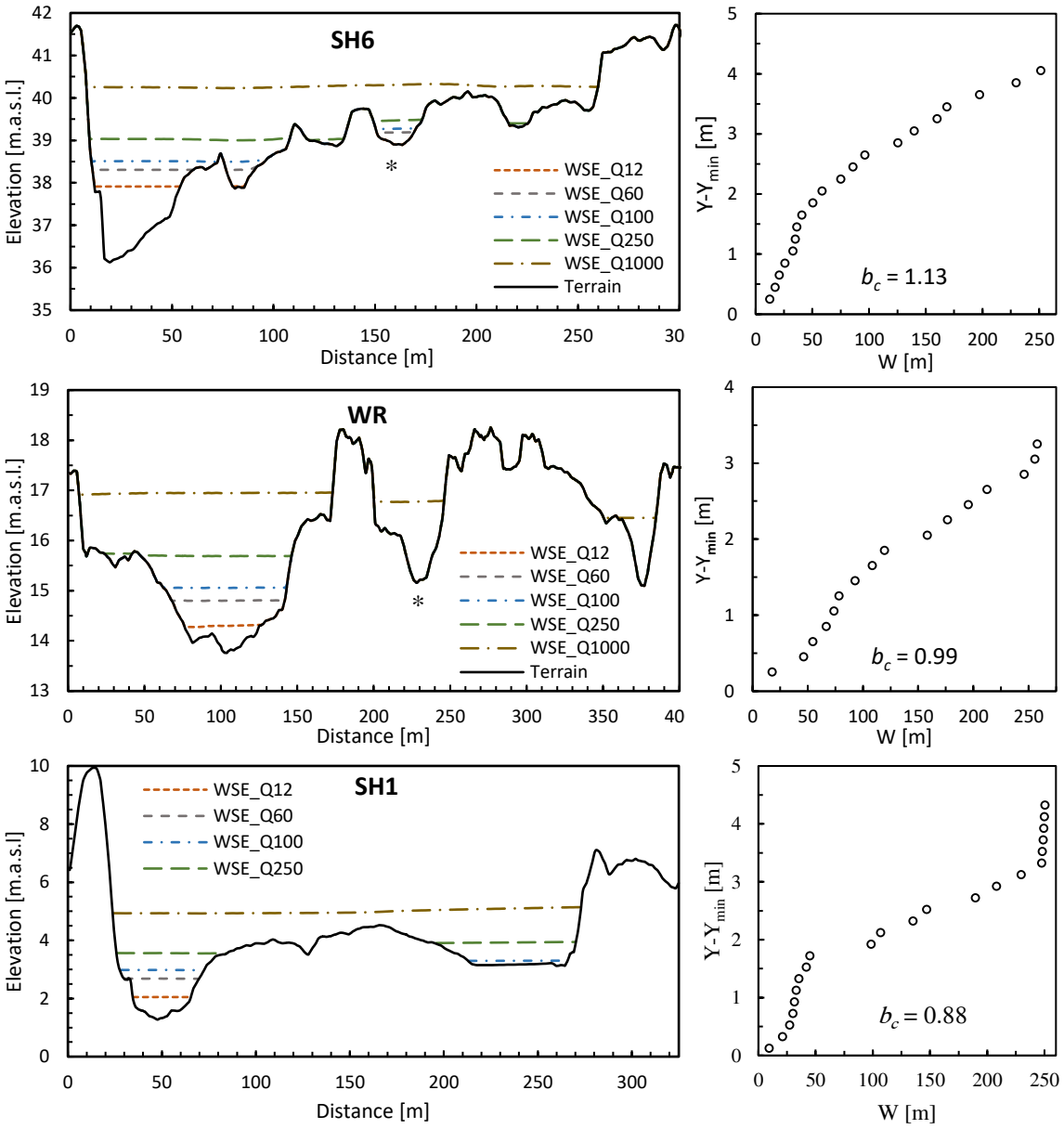


Figure 22 Water levels at the station's cross sections (left) and their shape exponent relationship (right)

At SH1, the low $b_c$ value indicates a stable spring-fed U-shape channel (Jowett, 1998) where the increase in width per height is confined by high riverbanks. Here, the linear width increase in the V-shaped main channel is balanced by the stagnant width increase in the rectangle shaped braid. The different width increase rates are clearly shown on the respective shape exponent plot.

Although $b_c$ is a useful index, it describes the channel geometry irrespective of how it is filled or other hydraulic properties. The simulation shows that the water level is not necessarily constant along the cross section. Flow distribution between the different braids in a certain cross-section does not depend only on the bed elevation of each braid. In SH6 for example, part of the 250 $m^3/s$ discharge is flowing in a braid (marked with an asterisk) where its bed elevation is higher than the water elevation in the main channel. At the same time in WR, this discharge is flowing only in the main channel even though the parallel braids have lower bed elevations than the water level. For such cases, the hydraulic geometry relationships provide better description for the cross section.

### 4.2.5 At-a-station hydraulic geometry relations

The hydraulic geometry relations for the previous cross sections, in addition to the upstream boundary condition cross section (RF), are plotted in figure (23) below. The power function equations (4 - 6) were derived and their coefficients and exponents are presented in table (4). At RF, the hydraulic exponents are more or less equally distributed between width, depth and velocity, with values between 0.31 and 0.34. In other words, the increase in flow is accommodated by equal change in flow width, depth and velocity. On the other hand, by comparing RF to the other stations, the width coefficient (intercept of the power function curve) is significantly higher than in the rest of the stations, while the depth coefficient is the lowest, indicating that for a given discharge RF has the biggest flow width and lowest flow depth.

As for SH6, the velocity exponent is much higher at 0.51 in favor of the depth exponent at only 0.14, meaning that increased flows at this station is accommodated by higher change in velocities rather than notable changes in flow depth. This result is attributed to the cross section geometry, where the discharge is divided between multiple small braids having small depth range but variable velocities. (see SH6 in figure 22). However, the small depth range is not to be confused for small depth values. The depth coefficient (intercept value) is the highest of all stations starting from average depth 0.84 m at Q = 12 $m^3/s$ up to 1.4 m at Q = 1000 $m^3/s$. The V-shaped braids maintain the high depth values at low flows.

Hydraulic geometry exponents for WR are a little bit balanced, with water surface width highest at 0.38 followed by the depth exponent and the least is velocity exponent at 0.23. Its coefficients are relatively low giving bigger range for hydraulic properties. Its power function curve is quite steep at low and mean discharges and stagnant at higher discharge. This is also attributed to its v-shaped main channel. By comparing it to the previous station (SH6), WR has slightly lower width per discharge rate but significantly higher depth per discharge and velocity per discharge increasing rate.

As for SH1, its width exponent is significantly high at 0.56. This is due to an abrupt width increase by the inclusion of a wide rectangle braid to the narrower main channel (see SH1 in figure 22). This change is evident on the hydraulic geometry plots at around Q = 80 $m^3/s$, where a spike is observed in the width-flow relationship and a concurrent plummet is observed for depth/velocity-flow relationships.

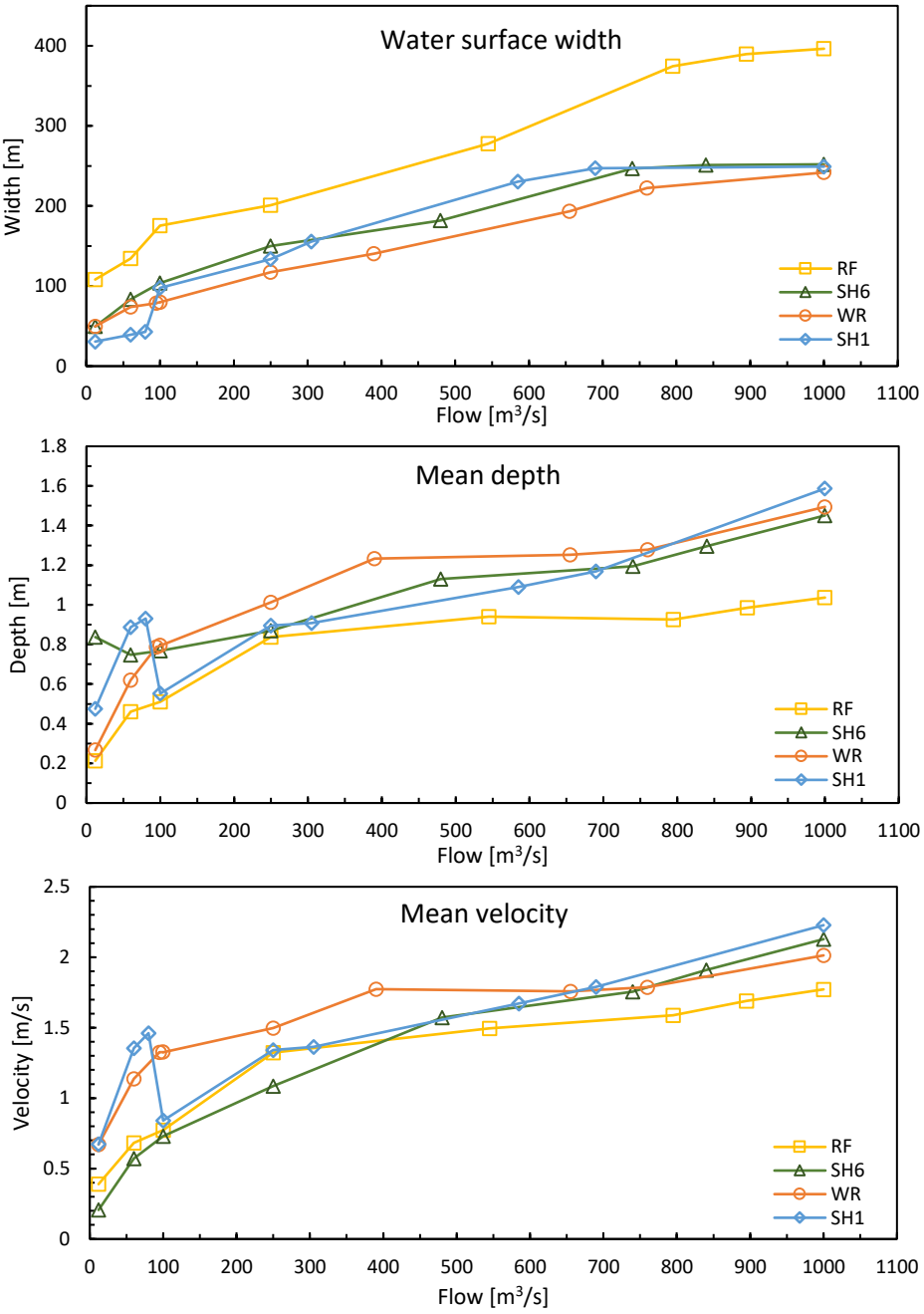


Figure 23 At-a-station hydraulic geometry relations

### 4.2.6 Reach averaged hydraulic geometry relations

Flow depth and velocity values were averaged in every reach separately at all simulated discharges. The water surface width is calculated for the reach by dividing the inundated water area by the main channel length. The resultant hydraulic geometry exponents and coefficients are shown in table (4) and compared to those of the stations. All hydraulic exponents gave close values across the three reaches. The average width exponent was 0.34, the average depth exponent was 0.28 and the average velocity exponent was 0.33. The main difference however was in the hydraulic coefficients of the power function relations (figure 24). Based on these coefficients, the Upper reach (RF-SH6) has the highest flow width and lowest flow depth per discharge value, the Lower reach (WR-SH1) has the highest flow depth and lowest flow

width per discharge, while the middle reach (SH6-WR) has average values for depth and width and a slightly higher velocity than the other two reaches.

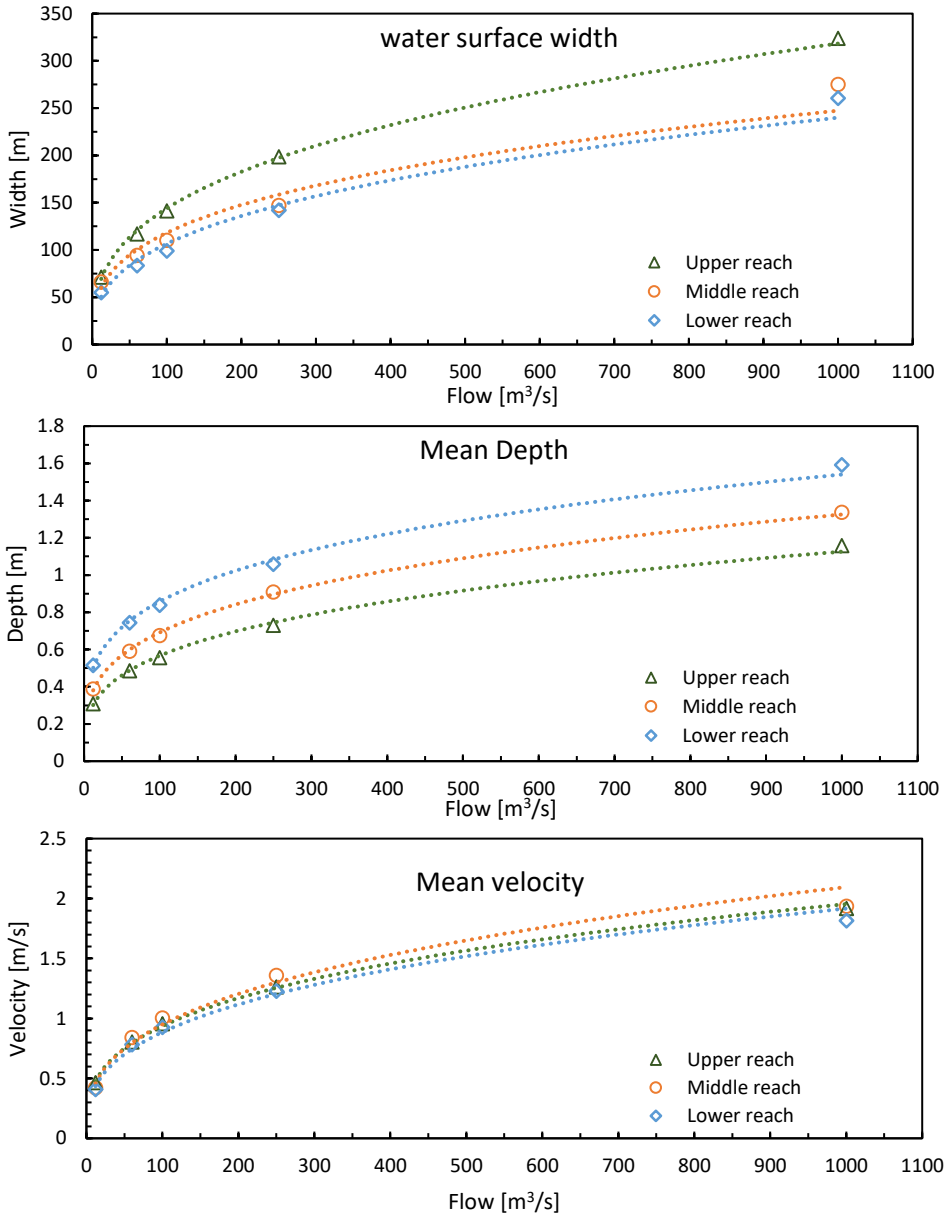


Table 4 Summary of the hydraulic relations' coefficients and exponents for the different stations and reaches

Figure 24 Reach averaged hydraulic geometry relations

| | | Hydraulic geometry coefficients | | | Hydraulic geometry exponents | | | Continuity eq. check | |
|---|---|---|---|---|---|---|---|---|---|
| | | a | c | k | b | f | m | a*c*k | b+f+m |
| At-a-station | RF | 42.786 | 0.104 | 0.168 | 0.311 | 0.342 | 0.344 | 0.748 | 0.997 |
| | SH6 | 18.117 | 0.484 | 0.065 | 0.384 | 0.136 | 0.509 | 0.569 | 1.029 |
| | WR | 16.159 | 0.134 | 0.432 | 0.376 | 0.358 | 0.226 | 0.939 | 0.959 |
| | SH1 | 5.675 | 0.283 | 0.420 | 0.562 | 0.221 | 0.224 | 0.675 | 1.007 |
| Reach averaged | Upper reach | 29.453 | 0.144 | 0.215 | 0.345 | 0.298 | 0.319 | 0.911 | 0.962 |
| | Middle reach | 26.991 | 0.189 | 0.194 | 0.321 | 0.282 | 0.344 | 0.989 | 0.947 |
| | Lower reach | 20.981 | 0.266 | 0.189 | 0.353 | 0.254 | 0.336 | 1.055 | 0.942 |

By comparing the hydraulic geometry relations derived at the stations with those derived for the reaches, the following differences are observed. Firstly, the exponents at a station are location specific and do not necessarily represent the preceded reach. Secondly, the exponents values have a wider range (0.14 – 0.56) and the variance in coefficients' values is also high. Moreover, when checking for the continuity condition using equation's (7,8), we find that the product of the coefficients is considerably less than unity for most stations (between 0.57 – 0.94). Nevertheless, the sum of exponents is close to unity (between 0.96 – 1.03). This indicates that for small discharge values, the continuity condition is not met and the power function relations are less reliable in hydraulics prediction.

On the other hand, the reach averaged hydraulic geometry relations are more homogeneous. The relation between width, depth and velocity exponents are consistent in all reaches, in the sense that the depth exponent is always less than the width and velocity exponents. Moreover, the variance for coefficients value is also relatively low and their product is closer to unity (between 0.91 – 1.06), making them more reliable in predicting hydraulics at low flow conditions. Thus for a complex braided river geometry, it is recommended to use reach averaged hydraulic geometry relations for prediction at bigger scale.

Jowett (1998) performed a study on 73 sites in New Zealand and summarized the hydraulic geometry exponents and the shape exponent in figure (25) below. The average exponents' values for the whole study area (marked in red lines) were compared to the regional values of Jowett's. Both the velocity and depth exponents were found to be less than the regional mode values while the width exponent is significantly higher (i.e. similar values are found at only 5 out of 72 sites). This finding indicates that the discharge increase in the study area leads to more water surface width increase compared to depth or velocity increase.

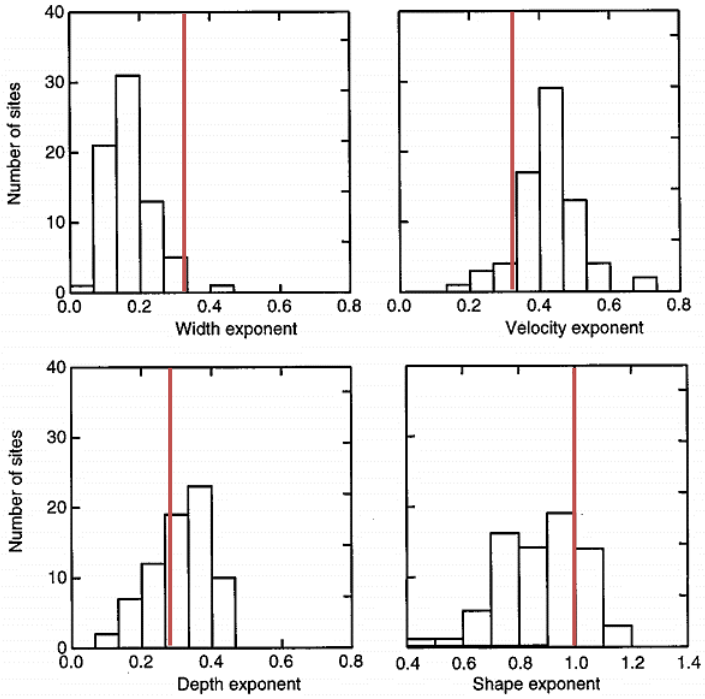


Figure 25 Simulated hydraulic geometry exponents compared to regional values

# 5 Conclusion and outlook

## 5.1 Conclusion

In this study, a 2D quasi-unsteady state hydraulic simulation was performed on a 23.5 km reach of the braided Wairau plains. The DEM geometry was corrected for water depth by means of Image derived bathymetry. The braiding intensity and sinuosity as well as the hydraulic geometry relations were derived for certain stations and reaches and compared with regional and international values. Based on the obtained results, the following conclusions were drawn:

The use of Aerial images in river bathymetry has a long history of successful applications were it can provide a near Lidar accuracy in optimum conditions. Although the liner equation adopted here uses only green and red bands of the visual light, but it demonstrated a good degree of robustness for predicting depth values ($R^2 = 0.744$; $\sigma_d = 0.206$ m). However, the relation also demonstrated systematic underestimation for high depth values (>1.25 m). Such behavior is logical since the dissipation of light in water column follows an exponential pattern. Therefore, it sets a limit for predicting depth after which the accuracy drops significantly. Here, the prediction of the maximum measured depth at 2.15 m incurred a 15% reduction. Apart from this method-inherited accuracy issue, the main uncertainty was using a LiDAR driven depth rather than actual measured depth to be compared with the image-derived depth. The quantification of this uncertainty was not possible due to lack of data. However, the flow at the times of LiDAR and Aerial photos was at base flow conditions, at which stage readings suggests minimal water-level fluctuations. Apart from that, few criteria should be met for acquiring the field data. An overcast, high-resolution aerial photo is recommended to be used and a uniform survey sampling (covering the depth range) is recommended in several literature (Legleiter, 2013; Moretto, Delai and Lenzi, 2013; Legleiter, Overstreet and Kinzel, 2018).

Secondly, the use of LiDAR and Aerial photos from different years (2014 and 2012 respectively) did not considerably affect the depth prediction, because the survey points used to derive the relation were filtered out in places of miss-alignments. However, when augmenting the LiDAR and the derived depth layer, the miss-aligned channel parts resulted in errors in the final geometry. As a volumetric balance, the volume that was initially filled by water in the original LiDAR is accurately predicted. Then this volume was assigned to different braids in the miss-aligned places. This caused few braid portions to be deeper and others to have water surface as their bed elevation. The main consequences of this problem were observed in the simulation results as hotspots of high shear stress values as well as decreasing the modal depth value. Overall, these miss-alignments are smaller in lengths considering the total study reach length, but the complex nature of the geometry makes it harder to measure its affect.

Coming to the 2D simulation results, the hydraulic geometry relations obtained facilitated a quantitative description of the dynamics in braided rivers, both at the cross-section and the reach scales. These relations are better understood when considering the associated channel shape (for cross sections) and the braiding intensity and sinuosity (for reaches). Overall, the braiding intensity is highest in the upper reach which is defined by several small V-shaped channels. The reach reacts to increased flows by increasing water surface width while the depth range remains small. At the middle reach, the braiding intensity decreases as braids converge and velocity builds up causing the highest channel sinuosity values. Then on the downstream reach, both braiding intensity and channel sinuosity are at their lowest

values. The channel is U-shaped and reacts to increased flows by increasing the depth while the water surface width stays relatively constant.

As for the comparison between reach-derived and station-derived hydraulic geometry relations, we find that the former were more consistent for all reaches and experience less variances in the exponents and coefficients values. Moreover, they score better in the continuity equation check. Therefore, reach averaged hydraulic exponents were compared to regional values (Jowett, 1998). The comparison result shows that the increase in water surface width per increasing flow is significantly higher than regional modal rates. The validation of these hydraulic relations was not easy due to difficulties in obtaining accurate and spatially representative field data (e.g. for bed roughness), especially at high flows. On the other hand, these uncertainties in field data had less effect on the frequency distribution of hydraulics in the bigger scales. The depth and velocity distributions followed similar positively skewed distribution patterns observed in other regional studies with comparable modal-to-mean ratio values (Mosley, 1982; Nicholas, 2003)

## 5.2 Further work

To validate these model results, the main sources of uncertainty should be tackled before future continuation in the study. Firstly, the river depth mapping should be validated using LiDAR and aerial photos within the same period. Elimination of the miss-alignment errors will allow for a better analysis of the shear stress and the stream power distribution. Secondly, the effect of spatial variations in the roughness values between channel bed and sand bars should be investigated as well as the temporal variation in the different seasons.

After revisiting those uncertainties, the next logical step would be to move from the quasi-state modelling to the full unsteady flow modelling. It will allow for a better understanding of some processes such as the peak flow dissipation, the wetting and drying and storage capacity of some braids. Another important aspect defining the hydraulics of braided rivers is the erosion and dispossession processes on the channel. Including a sediment transport model will help to explain further dynamics concerning the sand bars formation and the shifting of river channels. Lastly, the interaction between the river and the aquifer should be investigated properly by the use of a coupled model.

# 6 References


Arcement Jr., G. J. and Schneider, V. R. (1989) "Guide for Selecting Manning's Roughness Coefficients."

Ashmore, P. (2013) *Morphology and Dynamics of Braided Rivers*, *Treatise on Geomorphology*. Elsevier Ltd. doi: 10.1016/B978-0-12-374739-6.00242-6.

Casulli, V. (2009) "A high-resolution wetting and drying algorithm for free-surface hydrodynamics," *International Journal for Numerical Methods in Fluids*, 60(4), pp. 391–408. doi: 10.1002/fld.1896.

Chow, V. T. (1959) "Open-channel hydraulics," in *Open-channel hydraulics*. McGraw-Hill.

Christensen, K. and Doscher, C. (2010) "The interaction of river engineering and geomorphology in the Lower Wairau River, Marlborough, New Zealand," *Journal of Hydrology New Zealand*, 49(2), pp. 79–98.

CivilGEO (2019) *HEC-RAS 2D Flow Area Modeling*. Available at: https://www.civilgeo.com/knowledge-base/hec-ras-2d-flow-area-modeling/ (Accessed: August 7, 2019).

Davoren, A. and Mosley, M. P. (1986) "Observations of bedload movement, bar development and sediment supply in the braided Ohau river," *Earth Surface Processes and Landforms*, 11(6), pp. 643–652. doi: 10.1002/esp.3290110607.

Dierssen, H. M. *et al.* (2003) "Ocean color remote sensing of seagrass and bathymetry in the Bahamas Banks by high-resolution airborne imagery," *Limnology and Oceanography*, 48(1 II), pp. 444–455.

Gallant, J. and Basso, B. (2013) "Creating a flow-oriented modelling mesh using the stream function," in Piantadosi, J., Anderssen, R. S., and Boland, J. (eds.) *MODSIM2013, 20th International Congress on Modelling and Simulation*. Adelaide: Modelling and Simulation Society of Australia and New Zealand, p. 346. doi: EP139501.

Goff, J. R. and Ashmore, P. (1994) "Gravel transport and morphological change in braided sunwapta river, Alberta, Canada," *Earth Surface Processes and Landforms*, 19(3), pp. 195–212. doi: 10.1002/esp.3290190302.

Hoey, T. B. and Sutherland, A. J. (1991) "Channel morphology and bedload pulses in braided rivers: a laboratory study," *Earth Surface Processes and Landforms*, 16(5), pp. 447–462. doi: 10.1002/esp.3290160506.

Jowett, I. G. (1998) "Hydraulic geometry of New Zealand rivers and its use as a preliminary method of habitat assessment," *Regulated Rivers: Research & Management*, 14(5), pp. 451–466. doi: 10.1002/(sici)1099-1646(1998090)14:5<451::aid-rrr512>3.3.co;2-t.

Kim, J.-S. *et al.* (2010) "Roughness coefficient and its uncertainty in gravel-bed river," *Water Science and Engineering*. Hohai University. Production and hosting by Elsevier B.V., 3(2), pp. 217–232. doi: 10.3882/j.issn.1674-2370.2010.02.010.

Lane, S. N. and Richards, K. S. (1998) "High resolution, two-dimensional spatial modelling of flow processes in a multi-thread channel," *Hydrological Processes*, 12(8), pp. 1279–1298. doi: 10.1002/(SICI)1099-1085(19980630)12:8<1279::AID-HYP615>3.0.CO;2-E.

Legleiter, C. J. *et al.* (2004) "Passive optical remote sensing of river channel morphology and in-stream habitat: Physical basis and feasibility," *Remote Sensing of Environment*, 93(4), pp. 493–510. doi:

10.1016/j.rse.2004.07.019.

Legleiter, C. J. (2013) "MAPPING RIVER DEPTH FROM PUBLICLY AVAILABLE AERIAL IMAGES," *River Research and Applications*, 29(6), pp. 760–780. doi: 10.1002/rra.2560.

Legleiter, C. J., Overstreet, B. T. and Kinzel, P. J. (2018) "Sampling strategies to improve passive optical remote sensing of river bathymetry," *Remote Sensing*, 10(6), pp. 1–24. doi: 10.3390/rs10060935.

Legleiter, C. J., Roberts, D. A. and Lawrence, R. L. (2009) "Spectrally based remote sensing of river bathymetry," *Earth Surface Processes and Landforms*, 34(8), pp. 1039–1059. doi: 10.1002/esp.1787.

Leopold, L. B. and Maddock, T. (1953) *The hydraulic geometry of stream channels and some physiographic implications*, *U.S. Government Printing Office*. Washington, D.C. doi: 10.3133/pp252.

Lyzenga, D. R. (1978) "Passive remote sensing techniques for mapping water depth and bottom features," *Applied Optics*, 17(3), p. 379. doi: 10.1364/ao.17.000379.

McMillan, H. *et al.* (2010) "Impacts of uncertain river flow data on rainfall-runoff model calibration and discharge predictions," *Hydrological Processes*, 24(10), pp. 1270–1284. doi: 10.1002/hyp.7587.

Merwade, V. M., Maidment, D. R. and Hodges, B. R. (2005) "Geospatial Representation of River Channels," *Journal of Hydrologic Engineering*, 10(3), pp. 243–251. doi: 10.1061/(asce)1084-0699(2005)10:3(243).

Moretto, J., Delai, F. and Lenzi, M. A. (2013) "Hybrid DTMS derived by LiDar and colour bathymetry for assessing fluvial geomorphic changes after flood events in gravel-bed rivers (Tagliamento, Piave and Brenta Rivers, Italy)," *International Journal of Safety and Security Engineering*, 3(2), pp. 128–140. doi: 10.2495/SAFE-V3-N2-128-140.

Mosley, M. P. (1982) "Analysis of the effect of changing discharge on channel morphology and instream uses in a Braided River, Ohau River, New Zealand," *Water Resources Research*, 18(4), pp. 800–812. doi: 10.1029/WR018i004p00800.

Murray, A. B. and Paola, C. (1994) "A cellular model of braided rivers," *Nature*, 371(6492), pp. 54–57. doi: 10.1038/371054a0.

Nicholas, A. P. (2003) "Investigation of spatially distributed braided river flows using a two-dimensional hydraulic model," *Earth Surface Processes and Landforms*, 28(6), pp. 655–674. doi: 10.1002/esp.491.

Osterkamp, W. R. (1978) "Gradient, discharge, and particle-size relations of alluvial channels in Kansas, with observations on braiding," *American Journal of Science*, pp. 1253–1268. doi: 10.2475/ajs.278.9.1253.

Singh, V. (2003) "On the theories of hydraulic geometry," *International journal of sediment research*, 18(3), pp. 196–218.

Thomas, R. and Nicholas, A. P. (2002) "Simulation of braided river flow using a new cellular routing scheme," *Geomorphology*, 43(3–4), pp. 179–195. doi: 10.1016/S0169-555X(01)00128-3.

Warburton, J. (1996) "Active braidplain width, bed load transport and channel morphology in a model braided river," *Journal of Hydrology (NZ)*, 35(2), pp. 259–285.

Westaway, R. M., Lane, S. N. and Hicks, D. M. (2003) "Remote survey of large-scale braided, gravel-bed rivers using digital photogrammetry and image analysis," *International Journal of Remote Sensing*, 24(4), pp. 795–815. doi: 10.1080/01431160110113070.

Williams, R. D. *et al.* (2013) "Hydraulic validation of two-dimensional simulations of braided river flow

with spatially continuous aDcp data," *Water Resources Research*, 49(9), pp. 5183–5205. doi: 10.1002/wrcr.20391.

Wilson, S. and Wöhling, T. (2015) "Wairau River-Wairau Aquifer Interaction," (February).

Winterbottom, S. J. and Gilvear, D. J. (1997) "Quantification of channel bed morphology in gravel-bed rivers using airborne multispectral imagery and aerial photography," *Regulated Rivers: Research & Management*, 13(6), pp. 489–499. doi: 10.1002/(SICI)1099-1646(199711/12)13:6<489::AID-RRR471>3.0.CO;2-X.

Wöhling, T. *et al.* (2018) "Quantifying River-Groundwater Interactions of New Zealand's Gravel-Bed Rivers: The Wairau Plain," *Groundwater*, 56(4), pp. 647–666. doi: 10.1111/gwat.12625.

# 7 Appendix A

Location of New Zealand's studied reaches, Jowett (1998).

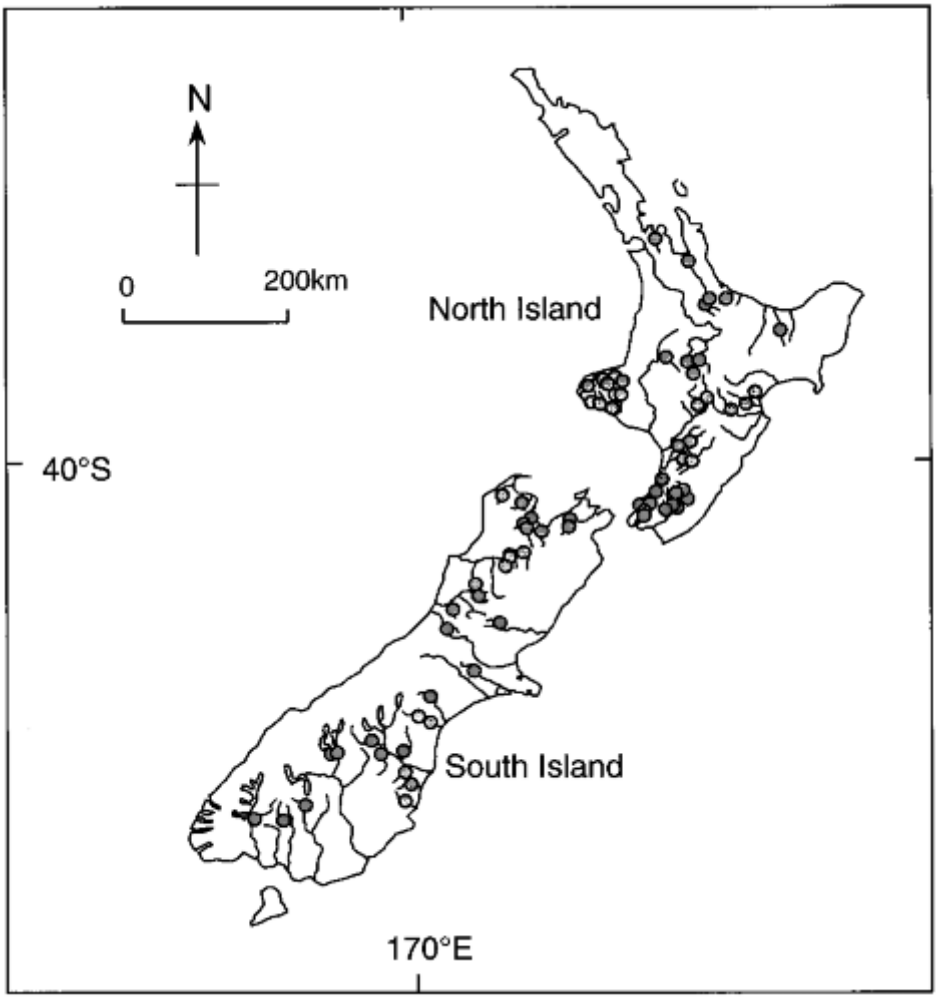

# 8 Appendix B

Table A.1. Hydraulic characteristics of 73 New Zealand river reaches at mean annual and mean annual minimum discharge, Jowett (1998)

| River | Mean annual discharge | | | | Mean annual minimum discharge | | | | Gradient | Channel shape exponent |
|---|---|---|---|---|---|---|---|---|---|---|
| | Flow ($m^3 s^{-1}$) | Width (m) | Depth (m) | Velocity ($m\ s^{-1}$) | Flow (m3 s-1) | Width (m) | Depth (m) | Velocity (m s-1) | | |
| **Ahuriri** | 23.7 | 46.9 | 0.58 | 0.86 | 8.5 | 37.5 | 0.39 | 0.58 | 0.005 | 0.9 |
| **Akatarawa** | 5.6 | 21 | 0.48 | 0.54 | 1 | 13.2 | 0.34 | 0.27 | 0.0027 | 1.03 |
| **Aorere** | 71.1 | 70.4 | 1.31 | 0.71 | 11.3 | 52.4 | 0.78 | 0.35 | 0.0026 | 0.84 |
| **Arnold** | 58 | 46.5 | 1.17 | 0.99 | 22.5 | 41.6 | 0.77 | 0.67 | 0.0013 | 0.95 |
| **Baton** | 7.7 | 21.7 | 0.53 | 0.63 | 1.6 | 18.4 | 0.26 | 0.32 | 0.0046 | 0.81 |
| **Buller** | 12.9 | 24.4 | 0.53 | 0.88 | 3.9 | 18.3 | 0.33 | 0.58 | 0.0084 | 0.82 |
| **Clutha** | 203.6 | 88.4 | 2.13 | 1.03 | 73.6 | 79.4 | 1.49 | 0.62 | 0.0012 | 0.78 |
| **Esk** | 5.5 | 16.4 | 0.48 | 0.65 | 2.1 | 14.3 | 0.33 | 0.44 | 0.0023 | 0.77 |
| **Gowan** | 26.6 | 31 | 0.87 | 0.82 | 9.5 | 24.3 | 0.56 | 0.59 | 0.0029 | 0.77 |
| **Grey** | 53.8 | 77.4 | 0.85 | 0.86 | 12.8 | 66.9 | 0.45 | 0.47 | 0.0033 | 0.97 |
| **Hakataramea** | 5.9 | 17.9 | 0.46 | 0.62 | 1 | 12.9 | 0.24 | 0.32 | 0.0034 | 0.77 |
| **Hawea** | 80 | 37.6 | 1.23 | 1.56 | 6 | 30.7 | 0.59 | 0.34 | 0.0042 | 0.69 |
| **Hurunui** | 25 | 40.4 | 0.72 | 0.76 | 8.2 | 33.1 | 0.46 | 0.45 | 0.0017 | 0.79 |
| **Hutt** | 22.4 | 30.2 | 0.85 | 0.82 | 2.1 | 20.8 | 0.41 | 0.29 | 0.0051 | 0.89 |
| **Inangahua** | 16.3 | 26.4 | 0.72 | 0.78 | 2.1 | 19 | 0.41 | 0.31 | 0.0045 | 0.79 |
| **Kakanui** | 5.2 | 23.1 | 0.6 | 0.4 | 0.3 | 16.3 | 0.37 | 0.1 | 0.0012 | 0.82 |
| **Kapoaiaia** | 1.1 | 8.4 | 0.33 | 0.4 | 0.3 | 7.2 | 0.18 | 0.23 | 0.018 | 1.14 |
| **Kapuni** | 1.8 | 12.4 | 0.34 | 0.48 | 0.4 | 9.2 | 0.24 | 0.29 | 0.0081 | 0.98 |
| **Kauaeranga** | 6.5 | 33.6 | 0.49 | 0.4 | 0.7 | 22.9 | 0.25 | 0.16 | 0.0031 | 0.98 |
| **Kaupokonui** | 3.1 | 13.4 | 0.42 | 0.54 | 0.7 | 10.6 | 0.25 | 0.27 | 0.0099 | 0.99 |
| **Kopuaranga** | 2.6 | 8.4 | 0.59 | 0.52 | 0.3 | 6.8 | 0.3 | 0.18 | 0.0021 | 0.67 |
| **Maerewhenua** | 3 | 14.9 | 0.33 | 0.55 | 0.6 | 10.9 | 0.17 | 0.28 | 0.0054 | 0.99 |
| **Mangahao** | 15.3 | 37.2 | 0.63 | 0.6 | 1.6 | 28.3 | 0.36 | 0.19 | 0.0012 | 1.01 |
| **Manganui** | 6.7 | 18.4 | 0.76 | 0.44 | 1.2 | 15 | 0.36 | 0.2 | 0.0072 | 1.14 |

Table A.1. (Continued)

| River | Mean annual discharge | | | | Mean annual minimum discharge | | | | Gradient | Channel shape exponent |
|---|---|---|---|---|---|---|---|---|---|---|
| | Flow ($m^3 s^{-1}$) | Width (m) | Depth (m) | Velocity ($m\ s^{-1}$) | Flow (m3 s-1) | Width (m) | Depth (m) | Velocity (m s-1) | | |
| **Mangaoraka** | 2.1 | 13.7 | 0.44 | 0.35 | 0.3 | 11.1 | 0.21 | 0.13 | 0.0043 | 1.18 |
| **Mangatainoka** | 17.2 | 35.6 | 0.84 | 0.55 | 1.4 | 25.7 | 0.46 | 0.17 | 0.0019 | 0.65 |
| **Mangles** | 9.9 | 18.7 | 0.67 | 0.75 | 2 | 14.5 | 0.4 | 0.37 | 0.004 | 0.75 |
| **Mararoa** | 34.2 | 36 | 0.95 | 1 | 8 | 26.1 | 0.65 | 0.54 | 0.0048 | 0.87 |
| **Mataura** | 18.8 | 29.5 | 0.81 | 0.8 | 5.3 | 25.2 | 0.52 | 0.47 | 0.0019 | 0.79 |
| **Maowhango** | 4 | 16.4 | 0.72 | 0.35 | 0.9 | 13.7 | 0.56 | 0.15 | 0.0016 | 0.53 |
| **Motueka** | 61 | 56.4 | 1.02 | 0.94 | 9.3 | 42.9 | 0.43 | 0.46 | 0.0026 | 0.95 |
| **Ngaruroro** | 17.6 | 26.2 | 0.91 | 0.66 | 4.1 | 19.5 | 0.72 | 0.34 | 0.0042 | 1.05 |
| **Ohau** | 6.4 | 27.8 | 0.39 | 0.55 | 1 | 17.2 | 0.23 | 0.29 | 0.0051 | 1.03 |
| **Opihi** | 5.7 | 19.1 | 0.58 | 0.48 | 1.1 | 14.5 | 0.36 | 0.25 | 0.0034 | 0.89 |
| **Opihi** | 19 | 33.1 | 0.61 | 0.84 | 3.4 | 25.1 | 0.31 | 0.41 | 0.0034 | 0.79 |
| **Orari** | 9.9 | 18.2 | 0.53 | 0.94 | 2.9 | 14.2 | 0.31 | 0.61 | 0.0076 | 0.84 |
| **Oreti** | 30.3 | 54.5 | 0.51 | 0.98 | 5 | 31.7 | 0.27 | 0.55 | 0.0038 | 1.07 |
| **Oroua** | 11.2 | 20.8 | 0.5 | 0.96 | 1.1 | 13.4 | 0.19 | 0.41 | 0.0044 | 0.92 |
| **Otaki** | 28.1 | 34.6 | 1.06 | 0.73 | 4.7 | 24.3 | 0.73 | 0.33 | 0.0045 | 0.93 |
| **Otematata** | 7.6 | 27.2 | 0.43 | 0.56 | 1.7 | 20.7 | 0.25 | 0.32 | 0.0043 | 0.81 |
| **Patea** | 5.2 | 13.1 | 0.64 | 0.61 | 0.8 | 9.7 | 0.31 | 0.27 | 0.0093 | 1.07 |
| **Pauatahanui** | 0.7 | 5.2 | 0.4 | 0.41 | 0.1 | 3.8 | 0.23 | 0.16 | 0.0028 | 0.78 |
| **Pelorus** | 20.6 | 45.3 | 1.05 | 0.45 | 2.1 | 31.5 | 0.6 | 0.16 | 0.002 | 0.83 |
| **Pohangina** | 17.3 | 27.9 | 0.71 | 0.88 | 2.2 | 21.1 | 0.36 | 0.4 | 0.0045 | 0.75 |
| **Rai** | 17.5 | 29.5 | 0.93 | 0.64 | 1.5 | 22.3 | 0.46 | 0.19 | 0.002 | 0.76 |
| **Rangitikei** | 20.1 | 43.2 | 0.52 | 0.71 | 4.9 | 26.4 | 0.31 | 0.52 | 0.0039 | 0.76 |
| **Riwaka** | 2.5 | 15.4 | 0.36 | 0.42 | 0.6 | 12.4 | 0.23 | 0.21 | 0.0035 | 0.95 |
| **Ruahamanga** | 10.1 | 19.9 | 1.09 | 0.58 | 1.1 | 14.7 | 0.87 | 0.18 | 0.0021 | 0.92 |
| **Ruahamanga** | 22.5 | 39.9 | 0.66 | 0.8 | 2.5 | 30.9 | 0.29 | 0.3 | 0.0092 | 1.02 |

Table A.1. (Continued)

| River | Mean annual discharge | | | | Mean annual minimum discharge | | | | Gradient | Channel shape exponent |
|---|---|---|---|---|---|---|---|---|---|---|
| | Flow ($m^3 s^{-1}$) | Width (m) | Depth (m) | Velocity ($m\ s^{-1}$) | Flow (m3 s-1) | Width (m) | Depth (m) | Velocity (m s-1) | | |
| **Selwyn** | 3.4 | 18 | 0.42 | 0.48 | 0.7 | 14.3 | 0.24 | 0.25 | 0.005 | 1.03 |
| **Shag** | 1.7 | 11.3 | 0.43 | 0.38 | 0.1 | 7.1 | 0.32 | 0.09 | 0.0015 | 0.9 |
| **Stony** | 6.4 | 15.8 | 0.55 | 0.61 | 2.2 | 11.2 | 0.47 | 0.43 | 0.0118 | 0.93 |
| **Taipo** | 43.3 | 42.2 | 0.79 | 1.16 | 12.8 | 32.5 | 0.51 | 0.71 | 0.0093 | 0.78 |
| **Takaka** | 14.9 | 33.7 | 0.62 | 0.59 | 1.6 | 19.4 | 0.26 | 0.3 | 0.0081 | 0.96 |
| **Tauherenikau** | 9 | 23.2 | 0.58 | 0.6 | 1.2 | 15.9 | 0.32 | 0.24 | 0.0042 | 0.94 |
| **Tauranga-Taupo** | 9.9 | 20.6 | 0.8 | 0.6 | 2.8 | 18.3 | 0.53 | 0.31 | 0.0008 | 0.71 |
| **Tawhiti** | 0.7 | 4.8 | 0.5 | 0.27 | 0.2 | 4.3 | 0.3 | 0.16 | 0.0015 | 0.63 |
| **Tongariro** | 11.6 | 34.3 | 0.53 | 0.57 | 3.2 | 20.6 | 0.39 | 0.41 | 0.0062 | 1.06 |
| **Tongariro** | 32.2 | 42.6 | 0.87 | 0.86 | 27.2 | 42.1 | 0.81 | 0.78 | 0.0071 | 0.78 |
| **Tutaekuri** | 16.1 | 35.8 | 0.54 | 0.68 | 3.4 | 22.4 | 0.32 | 0.45 | 0.0016 | 0.85 |
| **Waiari** | 4.2 | 9.8 | 1.01 | 0.41 | 3.8 | 9.7 | 0.98 | 0.38 | 0.0009 | 0.5 |
| **Waihou** | 5.5 | 11.8 | 0.76 | 0.6 | 4.8 | 10.8 | 0.76 | 0.61 | 0.0043 | 0.67 |
| **Waimakariri** | 5.1 | 11.9 | 0.56 | 0.66 | 3.9 | 11.3 | 0.49 | 0.61 | 0.0028 | 0.81 |
| **Waimana** | 7.6 | 28.4 | 0.45 | 0.59 | 1.4 | 18.5 | 0.27 | 0.32 | 0.0075 | 1.07 |
| **Waingawa** | 10.4 | 22.2 | 0.63 | 0.7 | 1.2 | 13.7 | 0.34 | 0.31 | 0.0076 | 0.95 |
| **Waingongoro** | 2.7 | 11.9 | 0.53 | 0.45 | 0.5 | 9.5 | 0.32 | 0.19 | 0.0078 | 0.93 |
| **Waiohine** | 31.2 | 47.6 | 0.77 | 0.78 | 8.2 | 39.1 | 0.52 | 0.42 | 0.0032 | 0.92 |
| **Waiongona** | 2.8 | 12.5 | 0.71 | 0.36 | 0.4 | 9 | 0.53 | 0.14 | 0.0117 | 1.01 |
| **Wairoa (Auckland)** | 2.8 | 9.6 | 0.58 | 0.65 | 2 | 21.6 | 0.47 | 0.24 | 0.0028 | 0.82 |
| **Wairoa (Nelson)** | 16.5 | 30.7 | 0.79 | 0.61 | 0.4 | 8.1 | 0.41 | 0.15 | 0.0017 | 1.04 |
| **Waiwakaiho** | 7.8 | 20.8 | 0.64 | 0.57 | 2.1 | 17 | 0.38 | 0.33 | 0.0158 | 1.08 |
| **Wanganui** | 27.5 | 55 | 0.6 | 0.77 | 8.7 | 45.1 | 0.36 | 0.49 | 0.005 | 1.06 |
| **Whakatiki** | 1.7 | 13.4 | 0.34 | 0.34 | 0.3 | 9.3 | 0.21 | 0.17 | 0.0047 | 0.99 |

# 9 Appendix C

Table A.2. Average values of the exponents b, f, and m gathered from literatures: Site specific, Jowett (1998)

| Source | Exponent | | | Drainage area | Conditions |
|---|---|---|---|---|---|
| | b | f | m | | |
| **Leopold and Maddock (1953** | 0.26 | 0.40 | 0.34 | Midwestern U. S. | |
| **Leopold et al. (1964)** | 0.26 | 0.40 | 0.34 | 158 stations in the U. S. A. | |
| | 0.12 | 0.45 | 0.43 | Brandywine River, Pennsylvania | |
| **Wolman (1955)** | 0.04 | 0.41 | 0.55 | | |
| **Leopold and Miller (1956)** | 0.26 | 0.33 | 0.32 | | |
| **Leopold and Langbein (1962)** | 0.23 | 0.42 | 0.36 | Circulating flume | Theoretical |
| **Langbein (1964)** | - | 0.50 | 0.50 | Stable river section | |
| | 0.23 | 0.42 | 0.35 | | |
| **Scott (1966)** | 0.35 | 0.42 | 0.55 | | Ephemeral streams |
| | 0.24 | 0.56 | 0.20 | Middlefork Salmon River near Cape Horn | Perennial streams |
| **Leopold and Skibitzke (1967)** | 0.16 | 0.30 | 0.52 | Bear Valley Creek near Cape Horn | 138 sq. Mi. |
| | 0.06 | 0.43 | 0.53 | Middlefork Salmon River near Meyers Cave | 180 sq. Mi. |
| | 0.04 | 0.36 | 0.61 | Big Creek near Big Creek | 2020 sq. Mi. |
| | 0.08 | 0.41 | 0.52 | Salmon River at Salmon | 470 sq. Mi. |
| | 0.27 | 0.20 | 0.53 | Salmon River at Challis | 2020 sq. Mi. |
| | 0.10 | 0.40 | 0.49 | 18 streams in the Appalachian Plateau | 3670 sq. Mi. |
| **Coates (1969)** | 0.36 | 0.20 | 0.44 | Baffin Island Sandurs | 13-61 sq. Mi. |
| **Church (1980)** | 0.22 | 0.31 | 0.48 | Big Sandy River, Kentucky | |
| **Stall and Yang (1970)** | 0.23 | 0.41 | 0.36 | Upper Holder Basin | |
| **Wilcox (1971)** | 0.09 | 0.36 | 0.53 | Fool Creek, Central Rocky Mountaimns | |
| **Heede (1972)** | -- | 0.43 | 0.52 | Ephemeral Streams in Semiarid U. S. A. | |
| | -- | 0.36 | 0.34 | Coast mountain streams, B. C., Canada | |
| **Ponton (1972)** | 0.21 | 0.32 | 0.50 | River dean at Addington Hall | |
| **Knighton (1972)** | 0.29 | 0.40 | 0.31 | Right distributory | Braided reach |
| | 0.11 | 0.56 | 0.33 | Left distributory | Braided reach |
| | 0.23 | 0.27 | 0.50 | Rocester | Braided reach |
| **Richards (1973)** | --- | 0.639 | 0.296 | Serlby Park | |
| | --- | 0.44 | 0.474 | Yaxall | |
| | --- | 0.37 | 0.57 | Draycott | |
| | --- | 0.576 | 0.32 | Beedly | |
| | --- | 0.342 | 0.603 | | |
| | --- | | 0.568 | | |
| | --- | | 0.583 | | |
| **Dury (1976)** | 0.543 | 0.344 | | | |

Table A.2. (Continued)

| Source | Exponent | | | Drainage area | Conditions |
|---|---|---|---|---|---|
| | b | f | m | | |
| **Riley (1978)** | 0.42 | 0.41 | 0.16 | Gwydir River | |
| | 0.35 | 0.48 | 0.17 | Namoi River | |
| | 0.35 | 0.52 | 0.13 | Barwon River | |
| | 0.38 | 0.46 | 0.16 | Three rivers | |
| **Williams (1978)** | 0.49 | 0.24 | 0.27 | | |
| **Betson (1979)** | 0.245 | | | Watersheds in Kentucky | |
| **Lane and Foster (1980)** | 0.375 | 0.375 | 0.25 | | |
| | 0.32 | 0.32 | 0.36 | | |
| **Abrahams (1984)** | 0.419 | -0.064 | 0.632 | West channel, 8 observations | |
| | -.671 | 0.863 | 0.753 | East channel: 8 observations | |
| **Philips and Harlan (1984)** | 0.367 | 0.049 | 0.580 | Blanca Meadow: 20 observations | |
| | 0.419 | -0.095 | 0.67 | West channel: 80 observations | |
| | -0.706 | 0.912 | 0.792 | East channel: 8 observations | |
| **Rhoads (1991)** | 0.50 | 0.34 | -- | Missouri River basin | 252 gaging stations |